MECHANICAL AND GEOMETRIC CONSIDERATIONS FOR THE AIRGAPLESS MOTOR

A Thesis

Submitted to the Faculty

of

Purdue University

by

Nathan W. Wheeler

In Partial Fulfillment of the

Requirements for the Degree

of

Master of Science in Electrical and Computer Engineering

August 2018

Purdue University

Indianapolis, Indiana

THE PURDUE UNIVERSITY GRADUATE SCHOOL
STATEMENT OF COMMITTEE OF APPROVAL

Dr. Euzeli Cipriano dos Santos Jr.

Department of Electrical and Computer Engineering

Dr. Steven Rovnyak

Department of Electrical and Computer Engineering

Dr. Lingxi Li

Department of Electrical and Computer Engineering

Approved by:

Dr. Brian King

Head of the Graduate Program

ACKNOWLEDGMENTS

A special thanks to the Electrical and Computer Engineering department. Through my collegiate career the ECE department has always given me opportunities to succeed and get the most out of my education. I would like to thank Dr. Euzeli Cipriano Dos Santos for giving me the opportunity to complete my graduate degree at IUPUI. His guidance, expertise, and mastery of topics regarding electric machines and power electronics inspired me to continue my education and write this thesis. I would also like to thank Dr. John Lee, Dr. Lingxi Li, and Dr. Steven Rovnyak. Through positions as a grader, tutor, teacher's aide, and research assistant, these professors believed in me enough to grant me an opportunity to give back to the campus that has given me so much. I would also like to thank Sherrie Tucker. Her guidance, kindness, and willingness to help were instrumental to completing this thesis. Other thanks goes to the many professors that were willing to bless me with knowledge over the course of my degree, fellow students I studied with for endless hours to pass an exam, and the university itself, which provided me an opportunity to earn my Masters.

TABLE OF CONTENTS

Page

LIST OF TABLES vi

LIST OF FIGURES vii

ABSTRACT ix

1 INTRODUCTION 1

1.1 History of the Airgapless Motor 1

1.2 Operating Principle of the Airgapless Motor 2

2 GEOMETRIC MODELING 6

2.1 Hypocycloidal Motion 6

2.2 Airgap Modeling 14

2.3 Angle of Action 18

3 ELECTRICAL MODELING 22

3.1 Magnetic Circuit 22

3.2 Inductances, Energy, and Torque 27

4 MECHANICAL MODELING 34

4.1 Mechanical Speed 34

4.2 Vector Analysis for Torque 37

4.3 Mechanical Energy 46

4.4 Tribology 48

5 CONTROL 52

5.1 Power Electronics 52

5.2 Choosing an Overlap Angle 54

6 SIMULATION AND RESULTS 56

6.1 Simulation 56

6.2 Prototypes 60

Page

7 SUMMARY 65
REFERENCES 66

LIST OF TABLES

Table Page

4.1 Lubrication types with respective λ. 49

5.1 Truth table for asymmetric bridge converter. 53

6.1 Values used for simulation of airgapless motor. 56

LIST OF FIGURES

Figure Page

1.1 C-core magnetic device (relay). 3

1.2 Cross sectional view of the proposed family of motor. 4

1.3 Pole excitation signals. 5

2.1 Hypocycloidal motion with internal rotor. 7

2.2 Plot of hypocycloidal motion with moving circle interior to stationary circle. 9

2.3 Hypocycloidal motion with external rotor. 10

2.4 Plot of hypocycloidal motion with moving circle exterior to stationary circle. 13

2.5 Geometry used for airgap expression. 14

2.6 Geometry used for airgap expression. 14

2.7 Plot of (2.22) versus (2.23) for several ratios of $r_s : r_r$. 16

2.8 Geometry used for generalizing airgap expression. 17

2.9 Angle of action for internal rotor. 18

2.10 Angle of action for external rotor 20

3.1 Airgapless motor with rotor internal to stator. 23

3.2 Equivalent circuit for airgapless motor. 24

3.3 Simplified equivalent circuit for calculating self inductance 27

3.4 Further simplified equivalent circuit for calculating self inductance 28

3.5 Simplified equivalent circuit for calculating mutual inductance. 30

3.6 Further simplified equivalent circuit for calculating mutual inductance. . . 31

3.7 Pole excitation signals. 32

4.1 Rotation of rotor about stator. 35

4.2 Force diagram for airgapless motor. 37

Figure Page

4.3 Change of angle δ with respect to motion. 41
4.4 Change of angle δ with respect to frictional force f_f. 42
4.5 Force diagram for airgapless motor with two active poles. 44
4.6 Pole excitation signals with overlap angle of α. 45
4.7 Rotational and vibratory movement of airgapless motor. 47
4.8 Asperities between two surfaces in contact. 48
4.9 Action of rolling wheel on surface. 50
5.1 Asymmetric bridge converter for driving airgapless motor. 52
5.2 One leg of asymmetric bridge converter for driving airgapless motor. . . . 53
5.3 Altered asymmetric bridge converter for driving airgapless motor. 54
5.4 Block diagram for feedback controller for airgapless motor. 55
6.1 Plots for $r_s : r_r = 15 : 14$, $n = 4$. 57
6.2 Plots for $r_s : r_r = 10 : 9$, $n = 4$. 58
6.3 Plots for $r_s : r_r = 15 : 14$, $n = 6$. 59
6.4 Plots for $r_s : r_r = 15 : 14$, $n = 6$. 60
6.5 Plot of torque versus time for $n = 50$. 61
6.6 Torque for a 6 phase airgapless motor with varying firing angle α. 62
6.7 Torque versus firing angle and input power for varying firing angles. 62
6.8 Plots for torque, voltage, and current for six phase device and sawtooth reference current. 63
6.9 Prototype motor with external rotor. 64
6.10 Multiphase internal rotor device. 64

ABSTRACT

Wheeler, Nathan W. M.S.E.C.E., Purdue University, August 2018. Mechanical and Geometric Considerations for the Airgapless Motor. Major Professor: Euzeli Cipriano dos Santos Jr.

The purpose of this thesis is to perform modeling from different perspectives for an airgapless motor. The airgapless motor is a proposed type of electric machine whose purpose is to replace hydraulic machines in low speed high torque applications. Because of the nature of the movement for this device, modeling of this device is atypical to the modeling done with other electric machines. This thesis will present the operating principle of the airgapless motor and take an analytical approach to modeling the torque and total energy in the device. In addition, this thesis will present the power electronics necessary to drive this device and offer recommendations to maximize the torque and minimize the torque ripple. MATLAB simulations are used to verify that the conclusion of this thesis are consistent with observations made by previous publications and prototypes.

1. INTRODUCTION

The objective of this thesis is to use geometry and vector analysis in order to model important quantities regarding a new type of electric device known as the airgapless motor. The model developed will be compared to approaches taken in previous publications. This thesis is divided into seven chapters. The first chapter will introduce the concept of the airgapless motor. The second chapter will explore the basic geometry of this device and obtain some important quantities related to the hypocycloidal motion. The third chapter will revisit and generalize the electrical modeling done in previous publications. The fourth chapter will discuss an alternative approach to calculating the torque using vector analysis and briefly discuss other important mechanical considerations. The fifth chapter will present the necessary power electronics to drive this device and recommend some control strategies to maximize average torque and minimize torque ripple. The sixth chapter will furnish results from simulations to verify the findings in chapters two through five, as well as present a few prototypes. The final chapter will summarize the findings in the preceding chapters. The author's main contributions to this thesis includes the geometric derivations involved in the electrical and mechanical modeling and the vector analysis for the static force, as well as the simulations done to verify that the static force matched the behavior of the prototypes.

1.1 History of the Airgapless Motor

An important consideration to designing electric machinery is how the characteristics of a machine will cater to the intended application. For example, three phase squirrel cage induction motors are desirable for industrial drives because of their ruggedness [1] [2]. Single phase induction motors are used in household appliances,

mainly because of their ability to run directly from a single-phase line [3] [4]. Synchronous motors, which operate at a constant speed, have a variety of applications as well, ranging from timing specific applications in both industrial and domestic settings [5] [6], to providing power factor correction to a large power systems [7] [8].

Even with the advancement of electric machinery over the last century, hydraulic motors are still employed for a variety of industrial applications. One of the primary reasons for a preference to hydraulic motors over electric motors is the ability to produce a large amount of torque compared to the total volume of the device [9] [10]. However, the drawbacks of hydraulic motors, including the low efficiency and requirement of a complex braking system, make it desirable to replace hydraulic machines with electrical machines in which these drawbacks are absent [11].

The concept of the airgapless motor has been explored as far back as 1961. Methodology to calculate the torque and total energy of the system, as well as minimizing the torque ripple, was explored in 1980 [12] [13]. The concept again appeared in 1995 as the rolling rotor switched reluctance motor [14]. The electrical modeling of the rolling rotor switched reluctance motor was explored extensively in 2009 [15] [16] [17] and again in 2017 [18] [19] [20]. The goal of the design of this machine is to provide a viable option of electric machinery for high torque, low speed applications. Applications can range from those that need high resolution and high torque, such as with a crane or a winch, to applications that use the vibrating motion to it's advantage, such as a shaker table, or maintenance of fine pipes [21].

1.2 Operating Principle of the Airgapless Motor

Most families of electric motors share a few key characteristics. One of the main similarities among most electric motors is that the rotor and stator are concentric to one another. As a result, an airgap is always present between the two. The presence of this airgap allows for the rotor to rotate freely. Although this airgap is fundamental for

transferring mechanical energy to electrical energy, designers typically try to minimize the size of the air gap in order to minimize the reluctance of the path of flux, which in turn maximizes the magnetic flux and consequentially the torque.

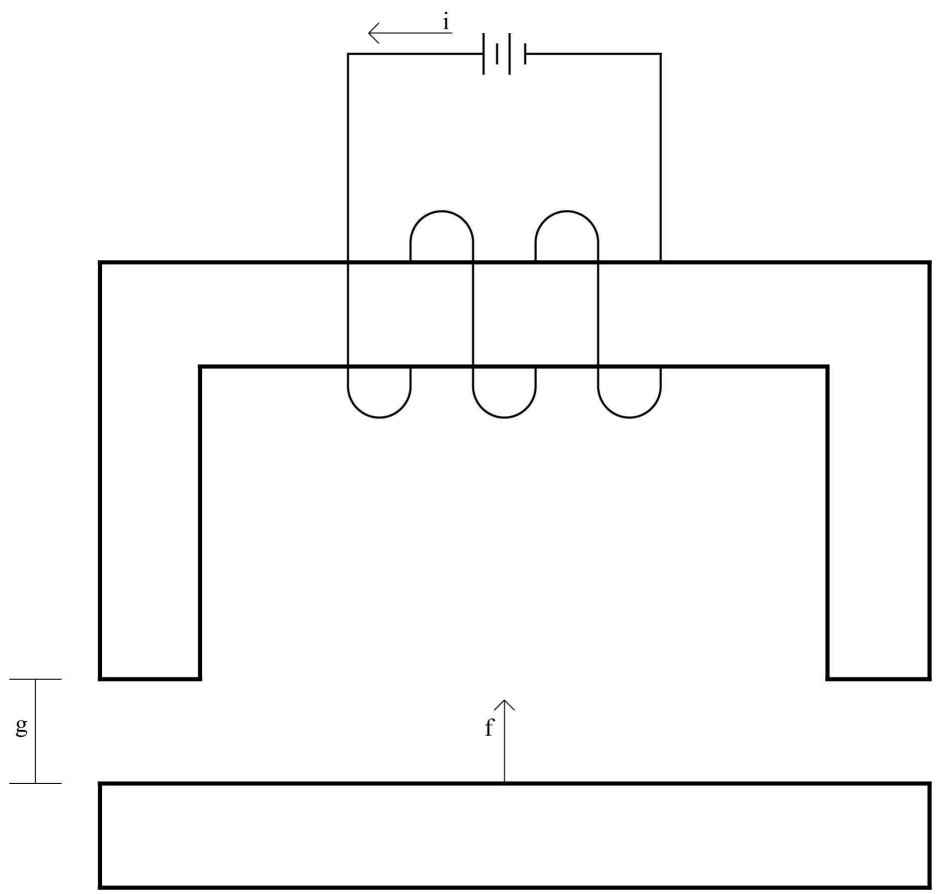

Fig. 1.1. C-core magnetic device (relay).

The proposed airgapless motor uses a similar concept as a relay. Consider the c-core relay presented in Fig. 1.1. As a direct current is applied to the coil, an attraction force is generated between the moving part and the stationary part. For a magnetic device such as this, the attraction force is directly proportional to the number of turns in the coil (N) and to the current (i), and inversely proportional to the gap (g). Ideally, as the gap between the moving and stationary parts of this

device approaches zero, the attraction force will approach infinity. However in real world applications, the gap will never reach zero because of the roughness between the two contacts.

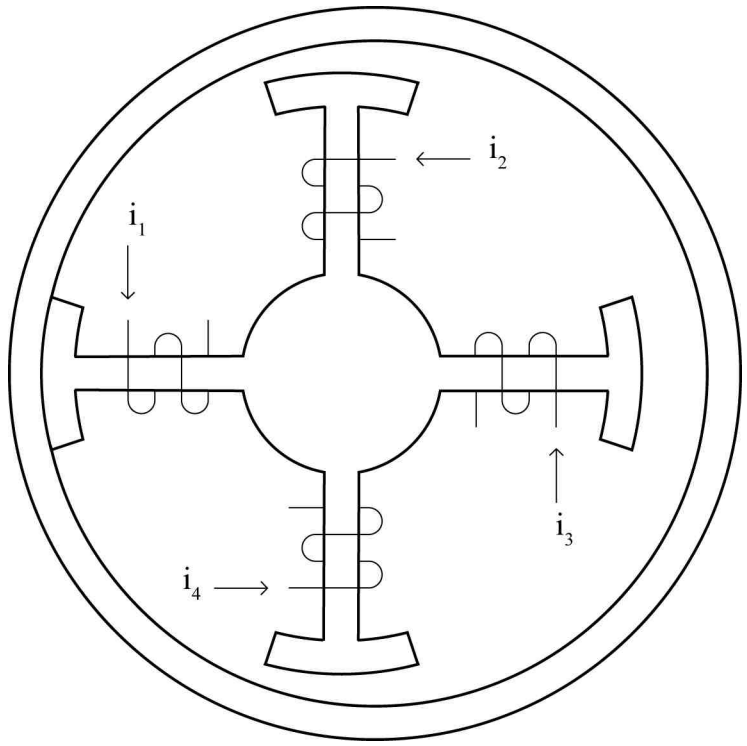

Fig. 1.2. Cross sectional view of the proposed family of motor.

For this proposed family of motors, the physical contact is used to its advantage to generate a large amount of attraction force and therefore rotational torque. The rotor is a cylindrical piece of material with high permeability such as 1040 steel. The stator is constructed such that each winding is equidistant from each other. A cross sectional view of this type of device is presented in Fig. 1.2. In this figure, the rotor is external to the stator. However, the operating principle is the same for when the rotor is internal to the stator. A DC voltage is applied to each pole of the stator one at a time, as seen in Fig. 1.3. As one pole is de-energized and voltage is applied to the subsequent pole, an attraction force is generated that causes the rotor to roll about

the stator. Although the figure presents a device with four poles, this concept can be applied to a device with as little as three poles or as many poles as will feasibly fit on the device.

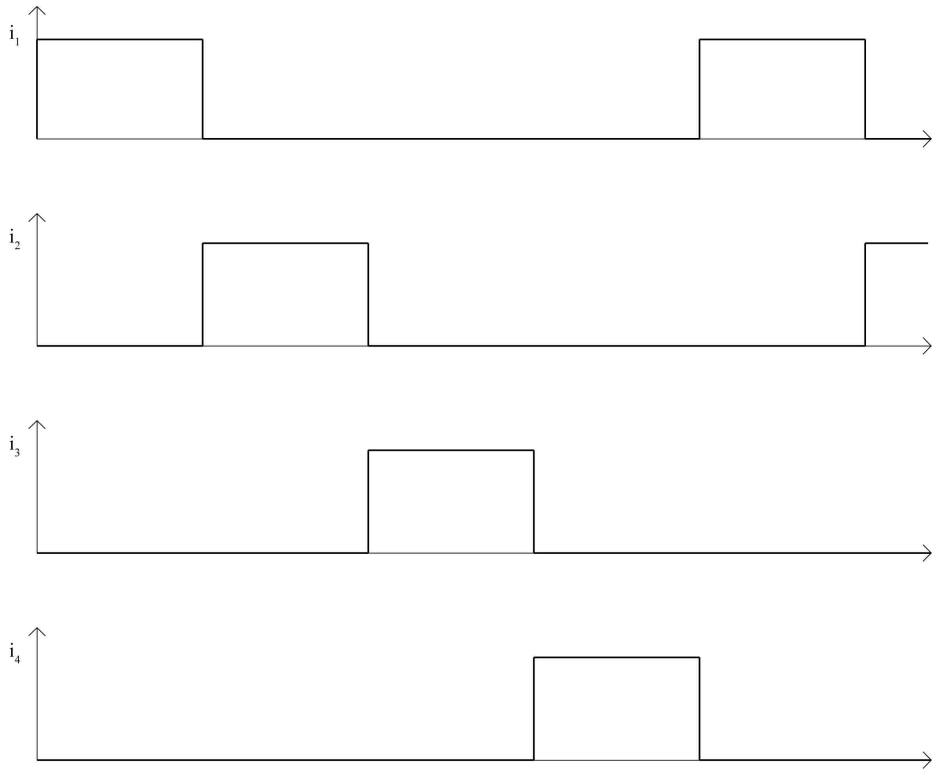

Fig. 1.3. Pole excitation signals.

Because the gap between the rotor and the stator is minuscule, the attraction force is immense. However, the combination of translational and rotational movement not present in other electric motors leads to interesting challenges regarding the mathematical modeling of this device. The goal of this thesis is to perform complex analysis and mathematical modeling from the perspective of several different fields.

2. GEOMETRIC MODELING

The airgapless motor presents challenges not seen in other electric machines because the rotor and stator are non-concentric to one another. Therefore, before approaching the modeling of this device to determine the equations for important variables such as mechanical speed and torque, is it important to take an in-depth look at the geometry of this device.

2.1 Hypocycloidal Motion

The motion of the airgapless motor is similar to the motion seen in a hypocycloid. In geometry, a hypocycloid is a special plane curve generated by the trace of a fixed point of a small circle within a large circle, as shown in Fig. 2.1 [22]. In this figure, the inner circle is rotating about the outer circle. The arc generated by the rolling contact between the two circles is highlighted in bold. The point C represents the center of the stationary circle. The point O represents the center of the moving circle. The point M represents the initial point of contact between the two circles on the outer stationary circle. The point P represents the initial point of contact between the two circles on the moving interior circle. The point M' represents the current point of contact between the two circles. The angle θ represents the angle $\angle MCM'$, or the angle generated by the arc between the initial and current point of contact with respect to the stationary circle. The angle ϕ represents the angle $\angle POM$, or the angle generate by the arc between the initial point of contact and the current point of contact with respect to the moving circle.

To generated the parametric equations for the hypocycloidal curve generated by point P, it is first necessary to describe the motion of point O about point C. The point O moves counterclockwise about the point C and generates a circle with a

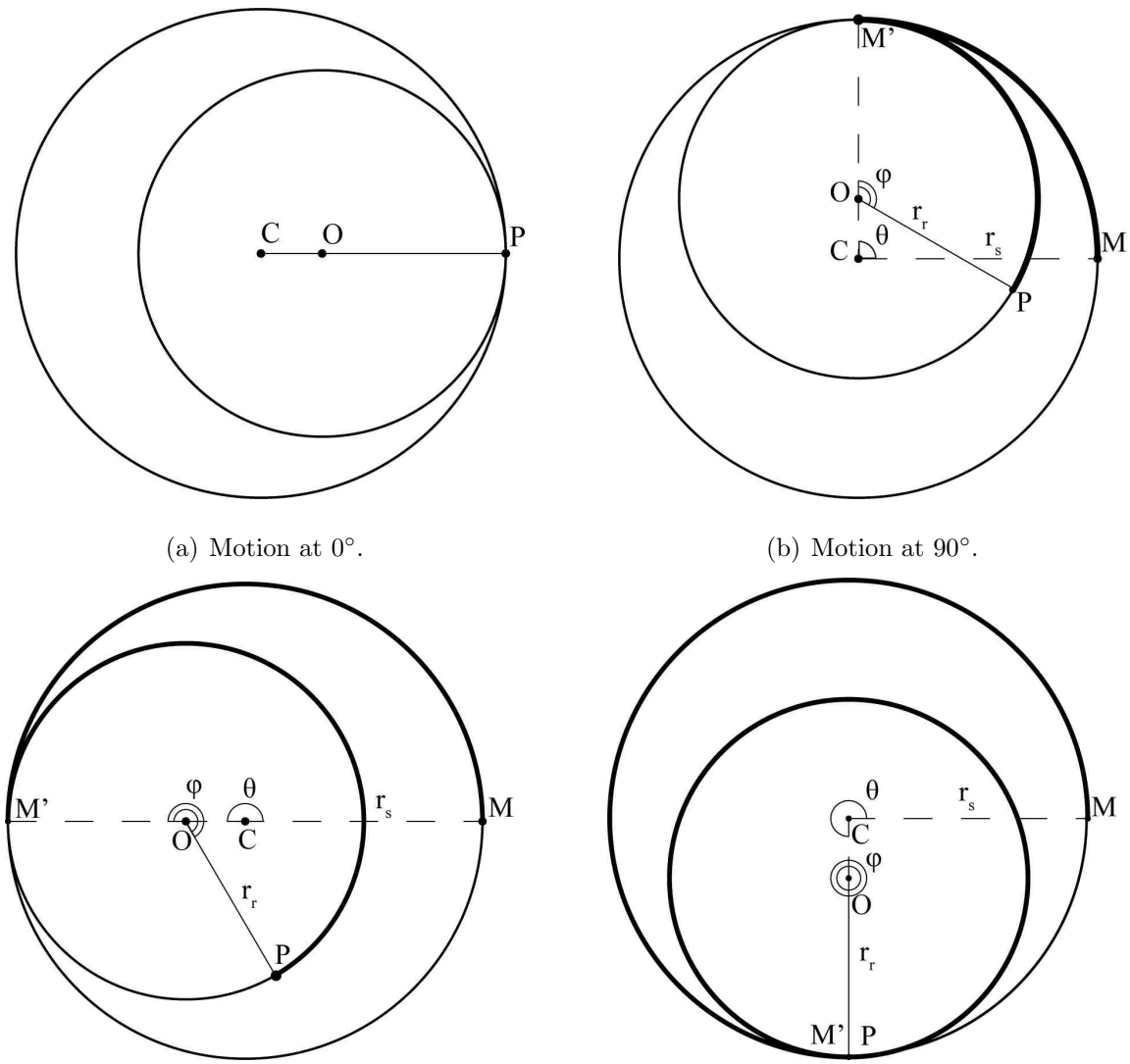

(a) Motion at 0°.

(b) Motion at 90°.

(c) Motion at 180°.

(d) Motion at 270°.

Fig. 2.1. Hypocycloidal motion with internal rotor.

radius of $r_{sr} = r_s - r_r$, where r_r is the radius of the moving circle and r_s is the radius of the stationary circle. The parametric equations that quantify the motion of point O about point C can be written as:

$$x_1(\theta) = r_{sr}\cos(\theta) \tag{2.1}$$

$$y_1(\theta) = r_{sr}\sin(\theta) \tag{2.2}$$

The inner circle is assumed to roll about the outer circle without slipping. Therefore the length of the arcs generated by angles θ and ϕ must be equivalent. Therefore, the following relationship holds:

$$s = r_r\theta = r_s\phi \tag{2.3}$$

$$\phi = \frac{r_s}{r_r}\theta \tag{2.4}$$

The next step is to quantify the motion of point P about point O. Over one complete revolution, the total motion of P about O is the difference between the angles ϕ and θ, or:

$$\phi - \theta = \frac{r_s}{r_r}\theta - \theta = \frac{r_s - r_r}{r_r}\theta = \frac{r_{sr}}{r_r}\theta \tag{2.5}$$

Point P moves clockwise about point O and generates a circle with a radius of r_r. The parametric equations that quantify the motion of point P about point O can be written as:

$$x_2(\theta) = r_r\cos(\phi - \theta) = r_r\cos\left(\frac{r_{sr}}{r_r}\theta\right) \tag{2.6}$$

$$y_2(\theta) = -r_r\sin(\phi - \theta) = -r_r\sin\left(\frac{r_{sr}}{r_r}\theta\right) \tag{2.7}$$

Point O is still moving about point C as point P is moving about point O. The parametric equations to quantify the movement of point P can be found via superposition:

$$x(\theta) = x_1 + x_2 = r_r\cos\left(\frac{r_{sr}}{r_r}\theta\right) + r_{sr}\cos(\theta) \tag{2.8}$$

$$y(\theta) = y_1 + y_2 = -r_r\sin\left(\frac{r_{sr}}{r_r}\theta\right) + r_{sr}\sin(\theta) \tag{2.9}$$

Fig. 2.2 presents plots of the hypo-cycloidal motion in which the moving circle is internal to the stationary circle for various ratios of r_r and r_s. In the figure, the ratio $r_s : r_r$ is, starting from the top left, 2:1, 3:2, 4:3, 5:4, 10:9, and 20:19 respectively.

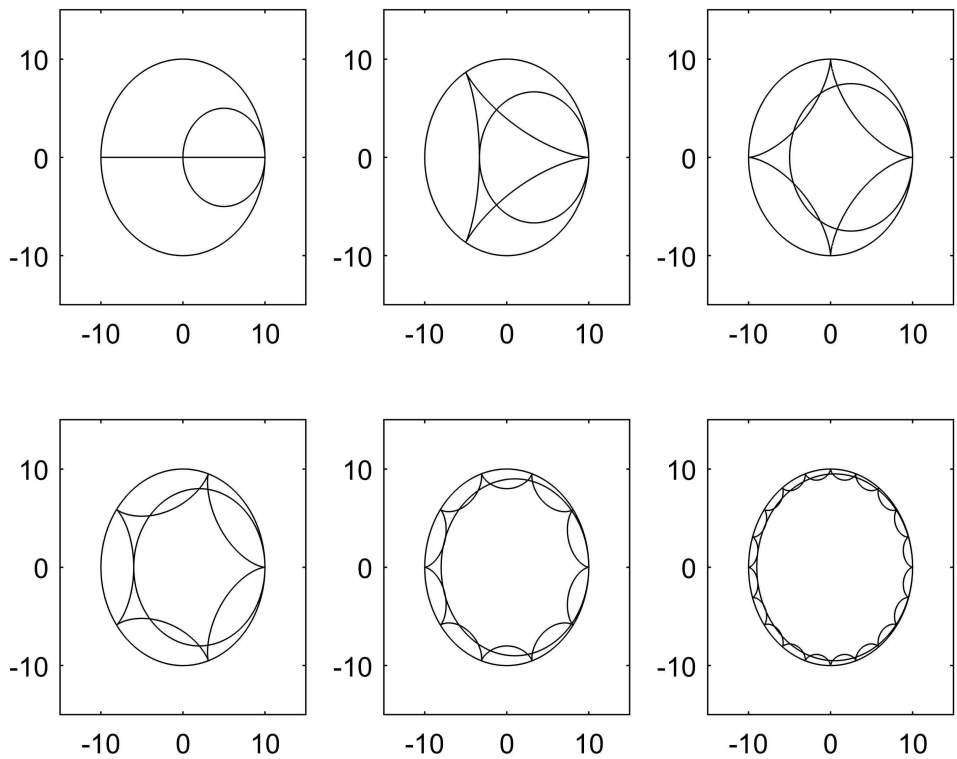

Fig. 2.2. Plot of hypocycloidal motion with moving circle interior to stationary circle.

A similar derivation can be performed when the outer circle is rotating about the stationary inner circle, as shown in Fig. 2.3. Points C, O, P, M, and M', as well as angles ϕ and θ, are defined in the same way that they are for the internal case seen above. In this case, point O still rotates counterclockwise about point P, generating a circle with a radius of $r_r - r_s = r_{rs} = -r_{sr}$.

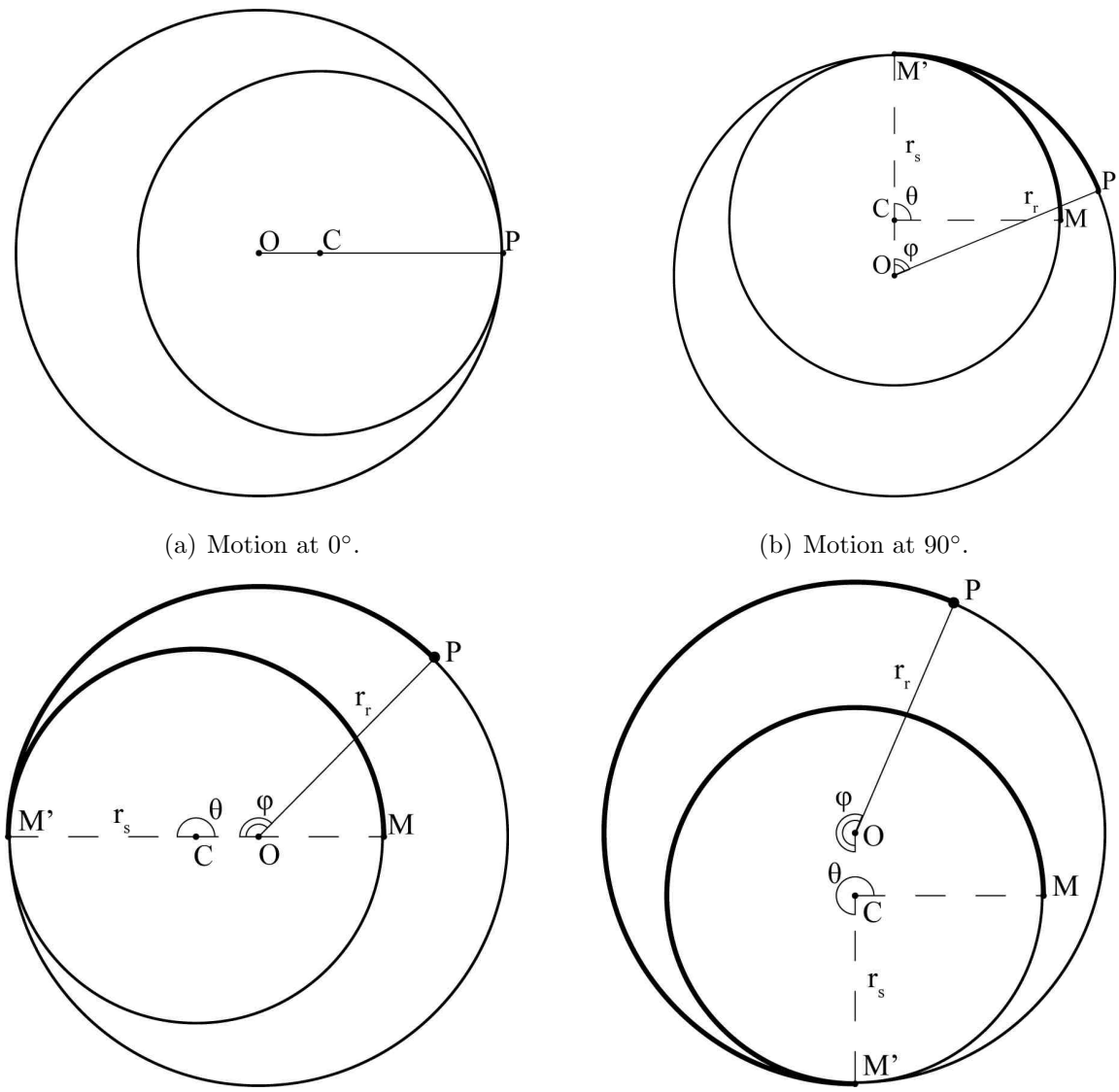

(a) Motion at 0°.

(b) Motion at 90°.

(c) Motion at 180°.

(d) Motion at 270°.

Fig. 2.3. Hypocycloidal motion with external rotor.

In the case where the external circle is rotating, point O begins at a position of 180° relative to point C. The parametric equations to describe the motion of point O about point C are given below:

$$x_1(\theta) = -r_{sr}\cos(\theta + \pi) = r_{sr}\cos(\theta) \tag{2.10}$$

$$y_1(\theta) = -r_{sr}\sin(\theta + \pi) = r_{sr}\sin(\theta) \tag{2.11}$$

As before, the outer circle is assumed to roll about the inner circle without slipping. Therefore, the lengths of the arcs generated by angles ϕ and θ are still equivalent, and the following relationship holds:

$$s = r_r\theta = r_s\phi \tag{2.12}$$

$$\phi = \frac{r_s}{r_r}\theta \tag{2.13}$$

The next step is to quantify the motion of point P about point O. From Fig. 2.3, over one complete revolution, the total motion of P about O is the difference between the angles θ and ϕ, or:

$$\theta - \phi = \theta - \frac{r_s}{r_r}\theta = \frac{r_r - r_s}{r_r}\theta = \frac{r_{rs}}{r_r}\theta = -\frac{r_{sr}}{r_r}\theta \tag{2.14}$$

Point P moves counterclockwise about point O and generates a circle with a radius of r_r. The parametric equations that quantify this motion are given below:

$$x_2(\theta) = r_r\cos(\theta - \phi) = r_r\cos\left(-\frac{r_{sr}}{r_r}\theta\right) = r_r\cos\left(\frac{r_{sr}}{r_r}\theta\right) \tag{2.15}$$

$$y_2(\theta) = r_r\sin(\theta - \phi) = r_r\sin\left(-\frac{r_{sr}}{r_r}\theta\right) = -r_r\sin\left(\frac{r_{sr}}{r_r}\theta\right) \tag{2.16}$$

As before, point O is still moving about point C as point P is moving about point O. The parametric equations to quantify the movement of point P can be found via superposition:

$$x(\theta) = x_1 + x_2 = r_r \cos\left(\frac{r_{sr}}{r_r}\theta\right) + r_{sr}\cos(\theta) \tag{2.17}$$

$$y(\theta) = y_1 + y_2 = -r_r \sin\left(\frac{r_{sr}}{r_r}\theta\right) + r_{sr}\sin(\theta) \tag{2.18}$$

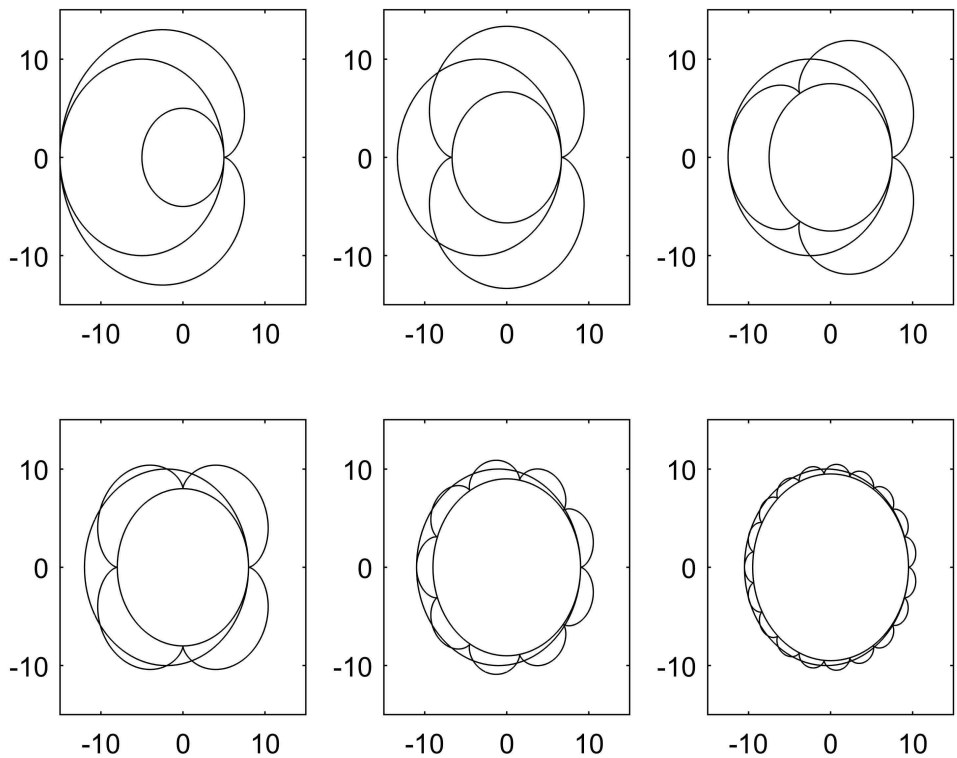

Fig. 2.4. Plot of hypocycloidal motion with moving circle exterior to stationary circle.

As seen above, the parametric equations to quantify the motion of point P about point C are identical, regardless of whether the rotating circle is internal or external to the stationary one. Fig 2.4 presents plots of the hypo-cycloidal motion in which the moving circle is external to the stationary circle for various ratios of r_r and r_s. In the figure, the ratio $r_s : r_r$ is, starting from the top left, 1:2, 2:3, 3:4, 4:5, 9:10, and 19:20 respectively.

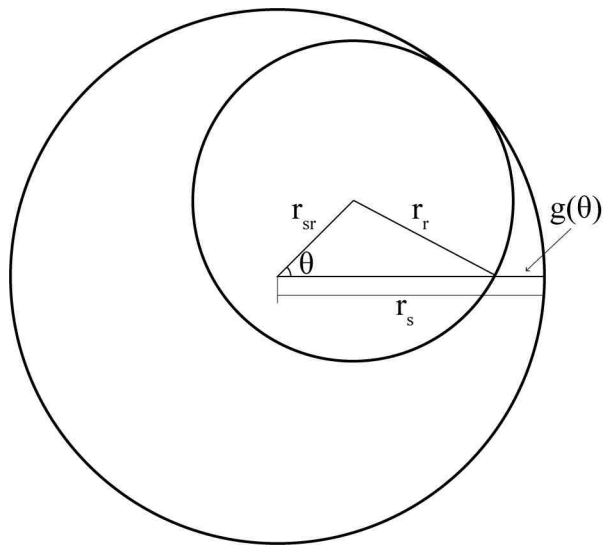

Fig. 2.5. Geometry used for airgap expression.

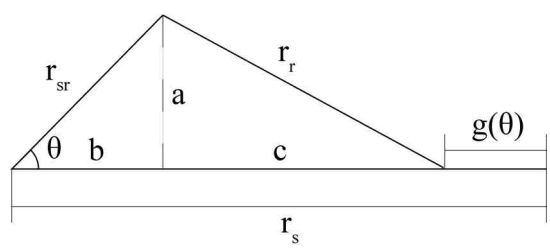

Fig. 2.6. Geometry used for airgap expression.

2.2 Airgap Modeling

As noted above, the key difference between the airgapless motor and other electric motors is that unlike other electric motors, the rotor and stator are not concentric. The variance of the airgap leads to difficulties with performing the modeling of key characteristics, such as force and torque. The first task with performing the modeling of these variables is to derive an expression for the air gap with respect to the angular position of the rotor. Consider Fig. 2.5.

In Fig. 2.5, the outer circle is stationary and considered to be the stator, while the inner circle is rolling about the outer circle, and is considered to be the rotor. When deriving the expression for the gap, it is also important to consider the path of the flux, which is expected to be normal to both surfaces. For this derivation, the gap will only be normal to the outer stationary circle.

Consider the triangle in Fig. 2.6. Intermediary variables a, b, and c are used to solve for the air gap as a function of the moving circle's displacement. Using simple trigonometric identities, a, b, and c can be found as:

$$a = r_{sr} sin(\theta) \tag{2.19}$$

$$b = r_{sr} cos(\theta) \tag{2.20}$$

$$c = \sqrt{r_r^2 - a^2} = \sqrt{r_r^2 - r_{sr}^2 sin^2(\theta)} \tag{2.21}$$

From Fig. 2.6, it is possible to use the intermediate variables to the geometry of the figure and therefore the air gap $g(\theta)$:

$$g(\theta) = r_s - c - b = r_s - \sqrt{r_r^2 - r_{sr}^2 sin^2(\theta)} - r_{sr} cos(\theta) \tag{2.22}$$

This device is most effective when the clearance between the two circles is very small, so when considering that $r_r \approx r_s$, the above simplifies to:

$$g(\theta) = r_s - r_r - r_{sr} cos(\theta) = r_{sr}[1 - cos(\theta)] = 2r_{sr} sin^2\left(\frac{\theta}{2}\right) \tag{2.23}$$

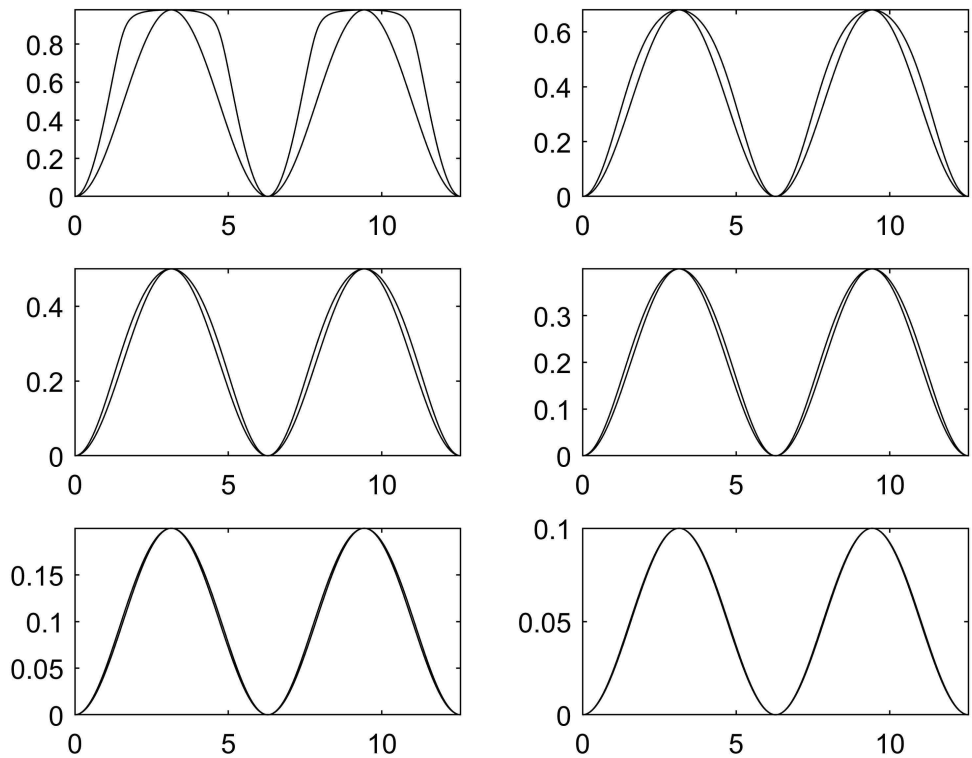

Fig. 2.7. Plot of (2.22) versus (2.23) for several ratios of $r_s : r_r$.

Fig. 2.7 shows the relation between (2.22) and (2.23) for ratios of $r_s : r_r$ of $2:1$, $3:2$, $4:3$, $5:4$, $10:9$, and $20:19$. As $r_s \rightarrow r_r$, these functions become more similar.

Now consider Fig. 2.8. In this figure, points a through h are spaced apart on the rim of the outer circle by 45°. If the outer circle is stationary and meant to represent the stator of the device, then the points a through h represent the poles, where a is the initial point of contact. It is possible to derive equations for the gap at any point:

$$g_a(\theta) = 2r_{sr}sin^2(0) \tag{2.24}$$

$$g_b(\theta) = 2r_{sr}sin^2(\frac{\pi}{8}) \tag{2.25}$$

$$g_c(\theta) = 2r_{sr}sin^2(\frac{\pi}{4}) \tag{2.26}$$

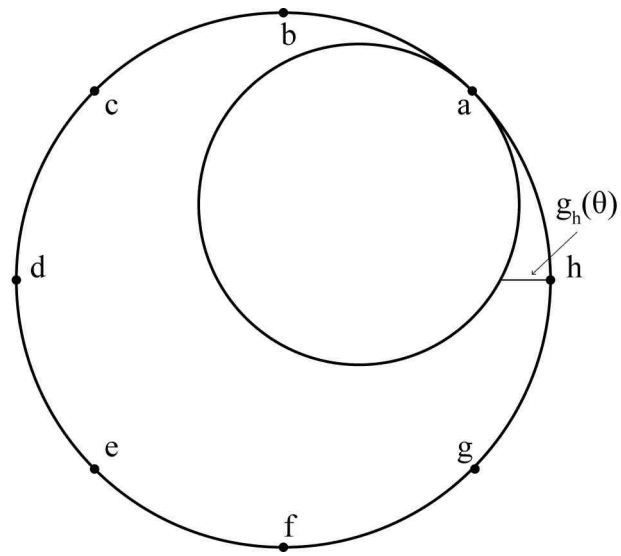

Fig. 2.8. Geometry used for generalizing airgap expression.

$$g_d(\theta) = 2r_{sr}sin^2(\frac{3\pi}{8}) \tag{2.27}$$

$$g_e(\theta) = 2r_{sr}sin^2(\frac{\pi}{2}) \tag{2.28}$$

$$g_f(\theta) = 2r_{sr}sin^2(\frac{5\pi}{8}) \tag{2.29}$$

$$g_g(\theta) = 2r_{sr}sin^2(\frac{3\pi}{4}) \tag{2.30}$$

$$g_h(\theta) = 2r_{sr}sin^2(\frac{7\pi}{8}) \tag{2.31}$$

From the above, it's possible to derive a general expression of the gap between the rotating inner circle in relation to the total number of points n, the angular position of the inner circle θ, and the difference between the two radii, r_{sr}.

$$g_k(\theta) = 2r_{sr}sin^2\left(\frac{\theta}{2} - \frac{(k-1)\pi}{n}\right) \tag{2.32}$$

For $k = 1, 2, 3, ..., n-1, n$.

2.3 Angle of Action

The angle of action δ is the angle between the point of contact and the next active pole on the stator with respect to the center of the rotor. δ will be vital to performing the vector analysis in chapter four.

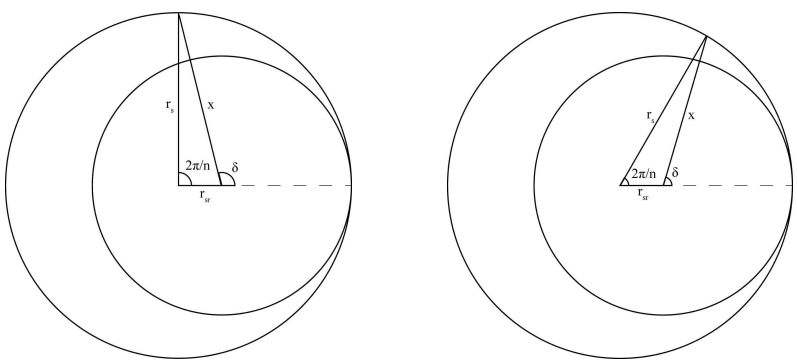

(a) δ at $\frac{360°}{n}$. with $n = 4$ (b) δ at $\frac{360°}{n}$. with $n = 6$

Fig. 2.9. Angle of action for internal rotor.

Refer to Fig. 2.9. To find this angle, yet another geometric exercise is necessary. First to find the unknown side x on the diagram. Through the law of cosines, x is given as:

$$x = \sqrt{r_s^2 + r_{sr}^2 - 2r_s r_{sr}\cos\left(\frac{2\pi}{n}\right)} \tag{2.33}$$

From (2.33), it is possible to use the law of sines in order to calculate the action of action δ:

$$\frac{\sin(\pi - \delta)}{r_s} = \frac{\sin(\delta)}{r_s} = \frac{\sin\left(\frac{2\pi}{n}\right)}{x} \tag{2.34}$$

Note that this only holds for $-90° \leq \delta \leq 90°$. When $\delta \leq 90°$, δ is given as:

$$\delta = \pi - \sin^{-1}\left(\frac{r_s \sin\left(\frac{2\pi}{n}\right)}{x}\right) = \pi - \sin^{-1}\left(\frac{r_s \sin\left(\frac{2\pi}{n}\right)}{\sqrt{r_s^2 + r_{sr}^2 - 2r_s r_{sr}\cos\left(\frac{2\pi}{n}\right)}}\right) \tag{2.35}$$

When $\delta > 90°$:

$$\delta = \sin^{-1}\left(\frac{r_s \sin\left(\frac{2\pi}{n}\right)}{x}\right) = \sin^{-1}\left(\frac{r_s \sin\left(\frac{2\pi}{n}\right)}{\sqrt{r_s^2 + r_{sr}^2 - 2r_s r_{sr}\cos\left(\frac{2\pi}{n}\right)}}\right) \tag{2.36}$$

Note that the unknown side x for an external rotor is also given by:

$$x = r_r + g(\delta) \tag{2.37}$$

The same method can be used to calculate the angle of action for when the rotor is external to the stator. Consider Fig. 2.10.

The unknown side x is found through the law of cosines.

$$x = \sqrt{r_s^2 + r_{rs}^2 - 2r_s r_{rs}\cos\left(\pi - \frac{2\pi}{n}\right)} = \sqrt{r_s^2 + r_{sr}^2 - 2r_s r_{sr}\cos\left(\frac{2\pi}{n}\right)} \tag{2.38}$$

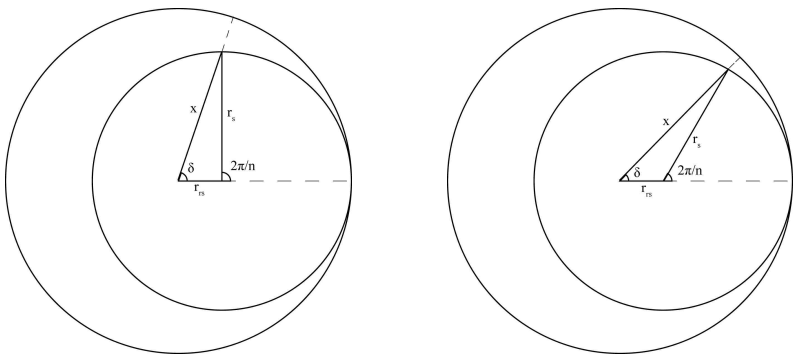

(a) δ at $\frac{360^\circ}{n}$ with $n = 4$. (b) δ at $\frac{360^\circ}{n}$ with $n = 6$.

Fig. 2.10. Angle of action for external rotor

And the angle of action δ is found through the law of sines.

$$\frac{\sin(\pi - \delta)}{r_s} = \frac{\sin(\delta)}{r_s} = \frac{\sin\left(\frac{2\pi}{n}\right)}{x} \tag{2.39}$$

as before, when $\delta \leq 90^\circ$, δ is given as:

$$\delta = \pi - \sin^{-1}\left(\frac{r_s \sin\left(\frac{2\pi}{n}\right)}{x}\right) = \pi - \sin^{-1}\left(\frac{r_s \sin\left(\frac{2\pi}{n}\right)}{\sqrt{r_s^2 + r_{sr}^2 - 2r_s r_{sr}\cos\left(\frac{2\pi}{n}\right)}}\right) \tag{2.40}$$

When $\delta > 90^\circ$, δ is given as:

$$\delta = \sin^{-1}\left(\frac{r_s \sin\left(\frac{2\pi}{n}\right)}{x}\right) = \sin^{-1}\left(\frac{r_s \sin\left(\frac{2\pi}{n}\right)}{\sqrt{r_s^2 + r_{sr}^2 - 2r_s r_{sr}\cos\left(\frac{2\pi}{n}\right)}}\right) \tag{2.41}$$

Note that the expression for δ is identical whether the rotor is internal or external to the stator. Also note that the unknown side x for an external rotor is also given by:

$$x = r_r - g\left(\delta\right) \tag{2.42}$$

This quantities will be used in chapter four when performing the vector analysis of the motor.

3. ELECTRICAL MODELING

As stated in the introduction, modeling for the airgapless motor has performed as recently as 2017 [18] [19] [20]. The goal of this section is to provide an up to date overview of the machine modeling for this particular device from an electrical perspective. Expressions for total energy and electromagnetic torque will be derived. These expressions will be compared to the conclusions made by the mechanical modeling in the following chapter. For a system with permanent magnets, the torque is defined via coenergy [23] [24].

3.1 Magnetic Circuit

Fig. 3.1 presents a four pole configuration of the airgapless motor with the rotor internal to the stator. Fig. 3.2 presents the equivalent magnetic circuit for this motor. In Fig. 3.2, R_r represents the reluctance of the rotor, R_s represents the reluctance of the stator, and R_{g1}, R_{g2}, R_{g3}, and R_{g4} represent the reluctance of the four airgaps. These reluctances can be easily found by the following:

$$R_r = \frac{l_r}{\mu_r A_r} \tag{3.1}$$

$$R_s = \frac{l_s}{\mu_s A_s} \tag{3.2}$$

$$R_{g1}(\theta) = \frac{g(\theta)}{\mu_o A_g} \tag{3.3}$$

$$R_{g2}(\theta) = \frac{g(\theta - \frac{\pi}{2})}{\mu_o A_g} \tag{3.4}$$

$$R_{g3}(\theta) = \frac{g(\theta - \pi)}{\mu_o A_g} \tag{3.5}$$

$$R_{g4}(\theta) = \frac{g(\theta - \frac{3\pi}{2})}{\mu_o A_g} \tag{3.6}$$

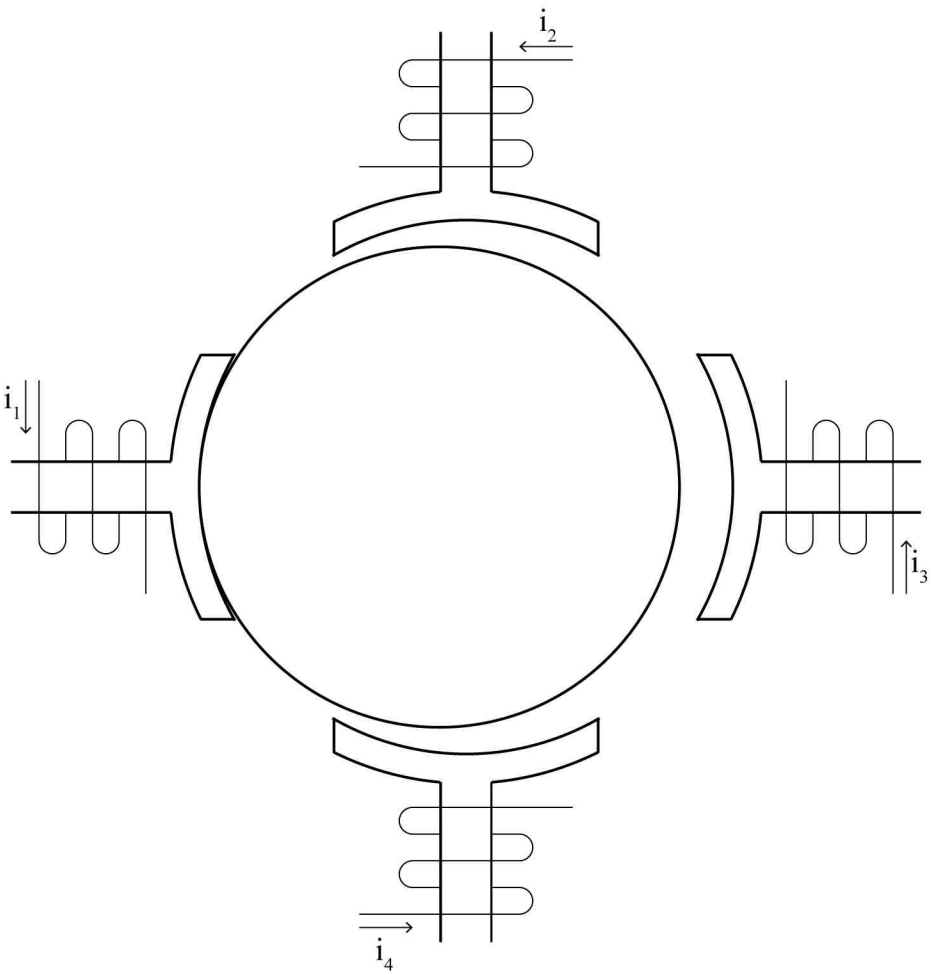

Fig. 3.1. Airgapless motor with rotor internal to stator.

In the above, l_r and l_s represents the length of the path of flux taken within the rotor and stator respectively. A_r and A_s represents the effective area of the path of flux taken within the rotor and the stator respectively. μ_r, μ_s, and μ_o represents the permeability of the material of the rotor, stator, and air.

Using Fig. 3.2, it is possible to relate the flux injection from each coil Φ_1, Φ_2, Φ_3, and Φ_4 with the mesh fluxes Φ_{12}, Φ_{23}, Φ_{34}, and Φ_{41} as follows:

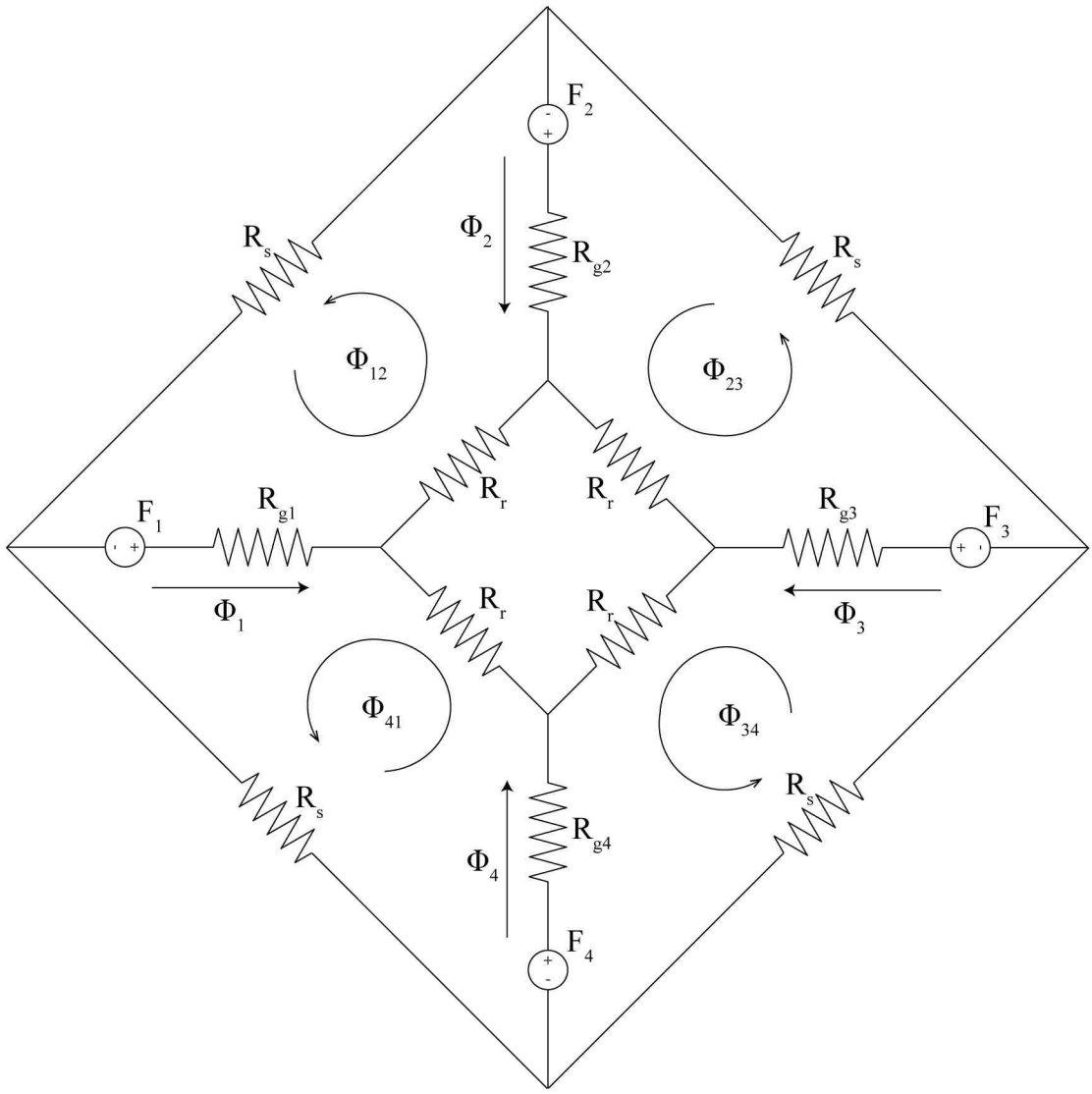

Fig. 3.2. Equivalent circuit for airgapless motor.

$$\begin{bmatrix} \Phi_1 \\ \Phi_2 \\ \Phi_3 \\ \Phi_4 \end{bmatrix} = \begin{bmatrix} 1 & 0 & 0 & -1 \\ -1 & 1 & 0 & 0 \\ 0 & -1 & 1 & 0 \\ 0 & 0 & -1 & 1 \end{bmatrix} \begin{bmatrix} \Phi_{12} \\ \Phi_{23} \\ \Phi_{34} \\ \Phi_{41} \end{bmatrix} \tag{3.7}$$

The relationship between the magneto-motive forces of each mesh and the mesh fluxes can be found as follows:

$$\begin{bmatrix} F_{12} \\ F_{23} \\ F_{34} \\ F_{41} \end{bmatrix} = \begin{bmatrix} R_{12} & -R_{g2} & 0 & -R_{g1} \\ -R_{g2} & R_{23} & -R_{g3} & 0 \\ 0 & -R_{g3} & R_{34} & -R_{g4} \\ -R_{g4} & 0 & R_{41} & -R_{g1} \end{bmatrix} \begin{bmatrix} \Phi_{12} \\ \Phi_{23} \\ \Phi_{34} \\ \Phi_{41} \end{bmatrix} \tag{3.8}$$

Where $R_{12} = R_r + R_s + R_{g1} + R_{g2}$, $R_{23} = R_r + R_s + R_{g2} + R_{g3}$, $R_{34} = R_r + R_s + R_{g3} + R_{g4}$, and $R_{41} = R_r + R_s + R_{g4} + R_{g1}$.

It is possible to expand the above into general terms based on the number of poles on the device. If there are n number of poles on the device, the airgaps are defined as:

$$g_k(\theta) = 2r_{sr} sin^2\left(\frac{\theta}{2} - \frac{(k-1)\pi}{n}\right) \tag{3.9}$$

for $k = 1, 2, 3, ..., n-2, n-1, n$. From this, it is possible to derive a general expression for the reluctances of each gap:

$$R_k(\theta) = \frac{g_k(\theta)}{\mu_o A_g} \tag{3.10}$$

The mesh fluxes in relation to the injection fluxes become:

$$\begin{bmatrix} \Phi_1 \\ \Phi_2 \\ \Phi_3 \\ \vdots \\ \Phi_{n-2} \\ \Phi_{n-1} \\ \Phi_n \end{bmatrix} = \begin{bmatrix} 1 & 0 & 0 & \dots & 0 & 0 & -1 \\ -1 & 1 & 0 & \dots & 0 & 0 & 0 \\ 0 & -1 & 1 & \dots & 0 & 0 & 0 \\ \vdots & \vdots & \vdots & \ddots & \vdots & \vdots & \vdots \\ 0 & 0 & 0 & \dots & 1 & 0 & 0 \\ 0 & 0 & 0 & \dots & -1 & 1 & 0 \\ 0 & 0 & 0 & \dots & 0 & -1 & 1 \end{bmatrix} \begin{bmatrix} \Phi_{12} \\ \Phi_{23} \\ \Phi_{34} \\ \vdots \\ \Phi_{(n-2)(n-1)} \\ \Phi_{(n-1)(n)} \\ \Phi_{n1} \end{bmatrix} \tag{3.11}$$

And a generalized expression for the magneto-motive forces in relation to the mesh fluxes becomes:

$$\begin{bmatrix} F_1 \\ F_2 \\ F_3 \\ \vdots \\ F_{n-2} \\ F_{n-1} \\ F_n \end{bmatrix} = \begin{bmatrix} R_{12} & -R_{g2} & 0 & \dots & 0 & 0 & -R_{g1} \\ -R_{g2} & R_{23} & -R_{g3} & \dots & 0 & 0 & 0 \\ 0 & -R_{g3} & R_{34} & \dots & 0 & 0 & 0 \\ \vdots & \vdots & \vdots & \ddots & \vdots & \vdots & \vdots \\ 0 & 0 & 0 & \dots & R_{(n-2)(n-1)} & -R_{g(n-1)} & 0 \\ 0 & 0 & 0 & \dots & -R_{g(n-1)} & R_{(n-1)(n)} & -R_{gn} \\ -R_{g1} & 0 & 0 & \dots & 0 & -R_{gn} & R_{n1} \end{bmatrix} \begin{bmatrix} \Phi_{12} \\ \Phi_{23} \\ \Phi_{34} \\ \vdots \\ \Phi_{(n-2)(n-1)} \\ \Phi_{(n-1)(n)} \\ \Phi_{n1} \end{bmatrix} \tag{3.12}$$

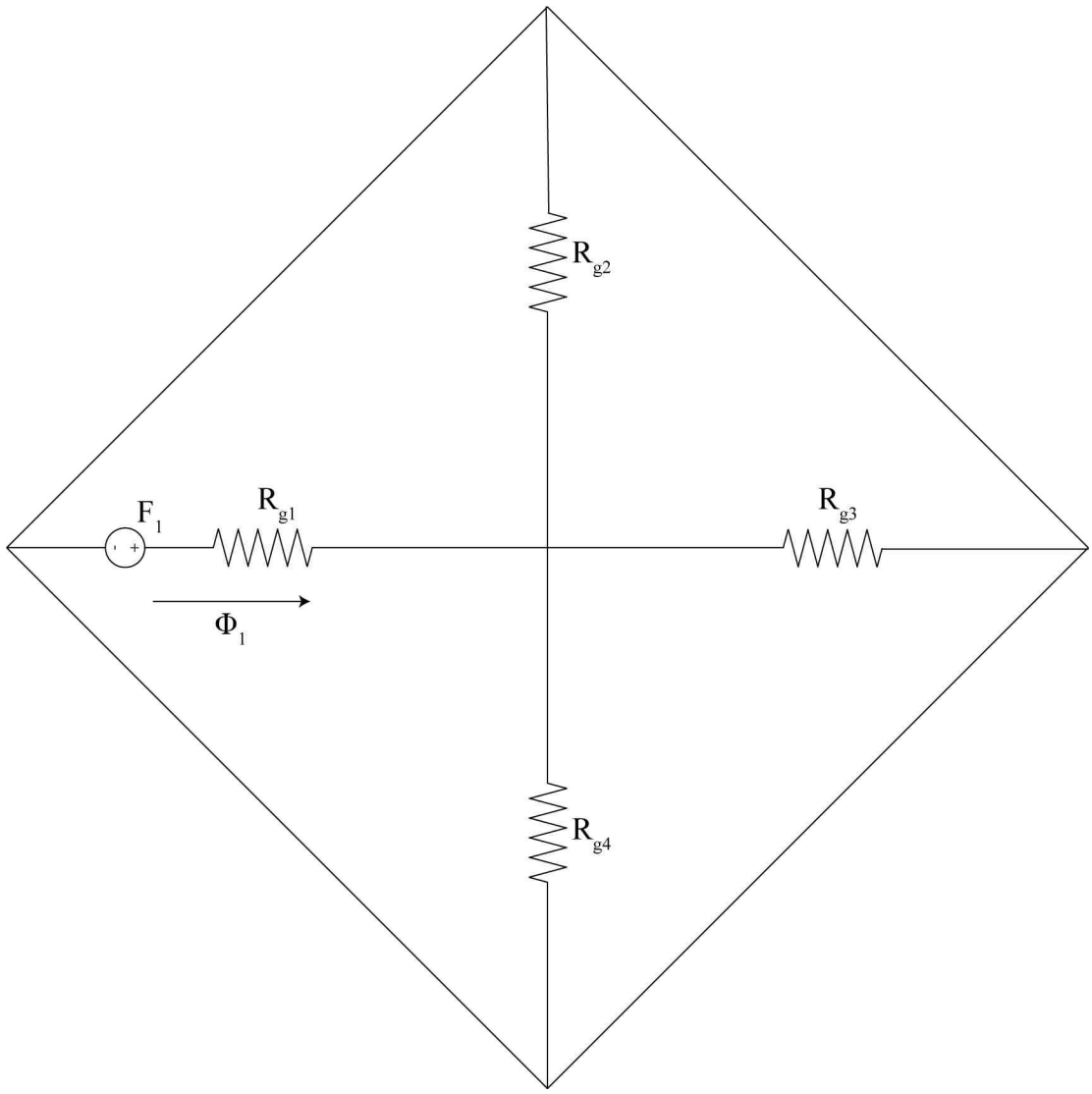

Fig. 3.3. Simplified equivalent circuit for calculating self inductance

Where the reluctances are defined similarly to how they are in (3.8).

3.2 Inductances, Energy, and Torque

Fig. 3.3 makes some simplifications to the circuit presented in Fig. 3.2. In Fig. 3.3, the reluctance of both the rotor and stator is considered to be negligible.

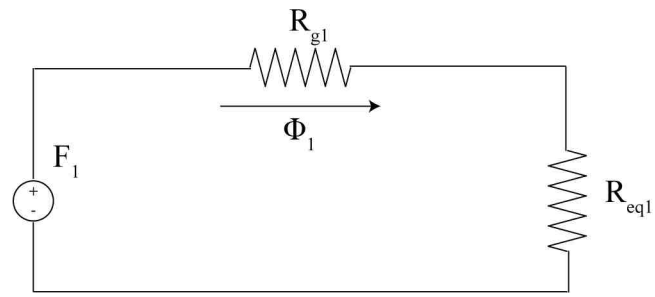

Fig. 3.4. Further simplified equivalent circuit for calculating self inductance

In Fig. 3.4, this circuit is further simplified as the magneto-motive force of the first pole F_1 in series with the reluctance of the gap at pole one R_{g1} and the equivalent reluctance of the remaining gaps R_{eq1}. R_{eq1} and the total reluctance R_{tot1} can be defined as:

$$R_{eq1} = \left(\frac{1}{R_{g2}} + \frac{1}{R_{g3}} + \frac{1}{R_{g4}} \right)^{-1} \tag{3.13}$$

$$R_{tot1} = R_{g1} + R_{eq1} \tag{3.14}$$

The reluctance seen at the other poles of the device, R_{tot2}, R_{tot3}, and R_{tot4}, can be calculated in a similar manner. Given the equivalent reluctance of the circuit above, it is possible to calculate the self inductance at pole one. By definition, the self inductance at pole one L_{11} is:

$$L_{11} = \frac{N\Phi_1}{i_1} = \frac{N^2}{R_{tot1}} \tag{3.15}$$

The flux flowing through pole 1 due to the other poles generate mutual inductances L_{12}, L_{13}, and L_{14}. These mutual inductances can be calculated in a similar manner to the self inductance found in (3.15). Refer to Fig. 3.5 and Fig. 3.6. In this figure, R_{eq12} is given as:

$$R_{eq12} = \left(\frac{1}{R_{g3}} + \frac{1}{R_{g4}} \right)^{-1} \tag{3.16}$$

And the mutual inductance L_{12} is found as:

$$L_{12} = \frac{N^2}{R_{eq12}||R_{g1}} \tag{3.17}$$

The mutual inductance L_{12} happens to be the same as the self inductance L_{22}. The mutual inductances L_{13} and L_{14} can be found in the same manner. Given the mutual inductances, it is possible to calculate the flux linkages as follows:

$$\lambda_1 = L_{11}i_1 + L_{12}i_2 + L_{13}i_3 + L_{14}i_4 \tag{3.18}$$

$$\lambda_2 = L_{21}i_1 + L_{22}i_2 + L_{23}i_3 + L_{24}i_4 \tag{3.19}$$

$$\lambda_3 = L_{31}i_1 + L_{32}i_2 + L_{33}i_3 + L_{34}i_4 \tag{3.20}$$

$$\lambda_4 = L_{41}i_1 + L_{42}i_2 + L_{43}i_3 + L_{44}i_4 \tag{3.21}$$

With the flux linkages, it is possible to calculate the voltage across each circuit:

$$v_1 = r_1 i_1 + \frac{d\lambda_1}{dt} \tag{3.22}$$

$$v_2 = r_2 i_2 + \frac{d\lambda_2}{dt} \tag{3.23}$$

$$v_3 = r_3 i_3 + \frac{d\lambda_3}{dt} \tag{3.24}$$

$$v_4 = r_4 i_4 + \frac{d\lambda_4}{dt} \tag{3.25}$$

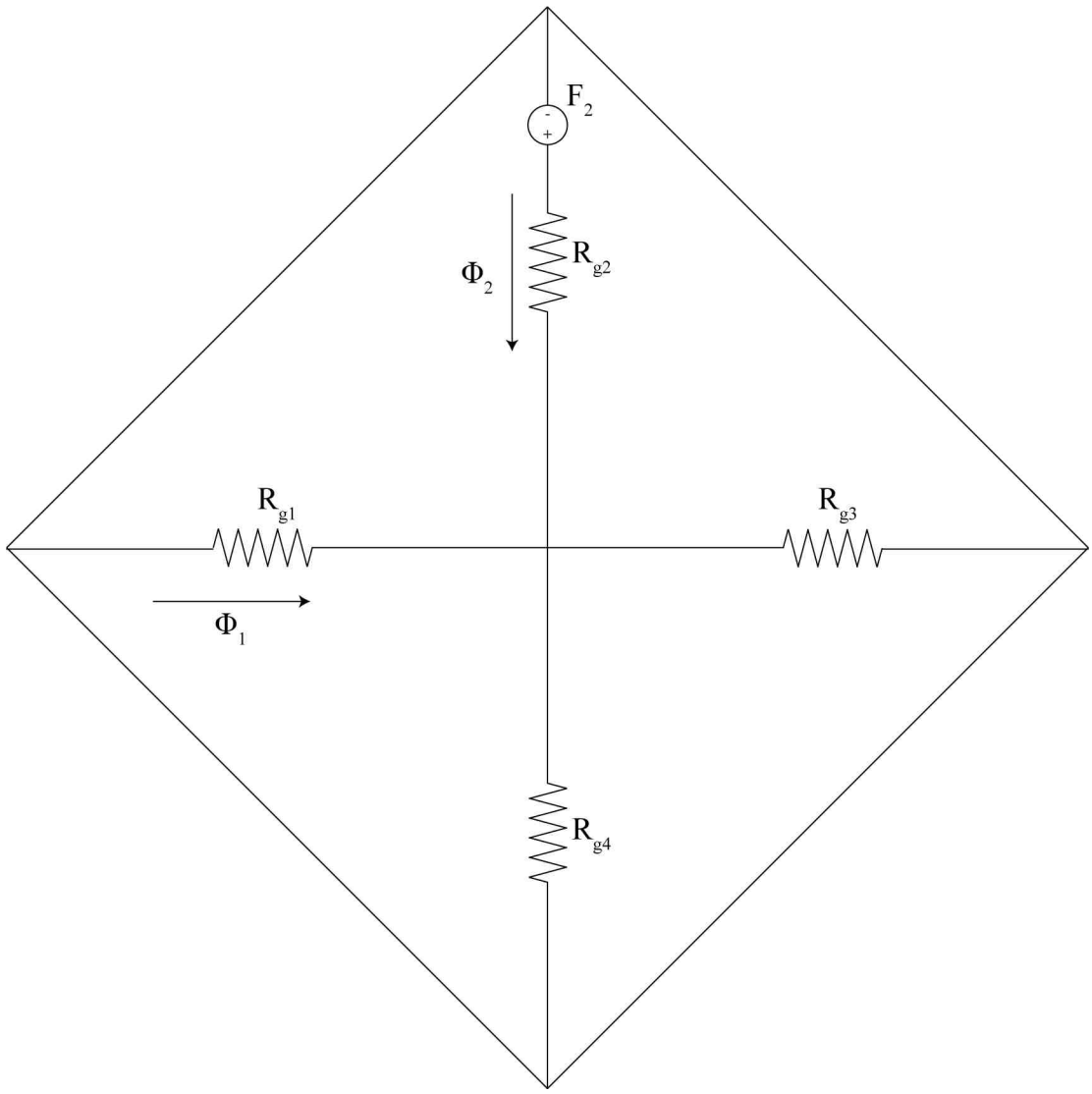

Fig. 3.5. Simplified equivalent circuit for calculating mutual inductance.

The flux linkages and voltages are known quantities, so the current can be found via (3.22) (3.23), (3.24), and (3.25). With the currents and flux linkages defined, it is possible to calculate the total energy of the system.

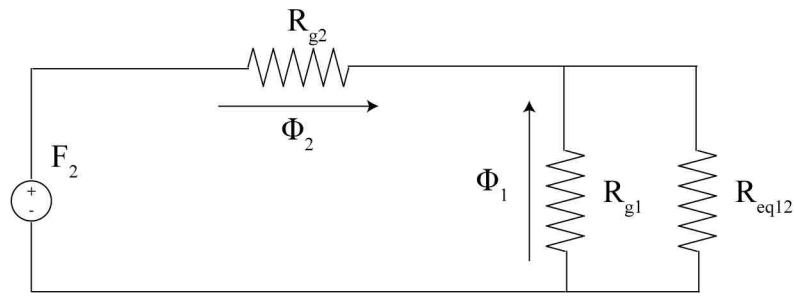

Fig. 3.6. Further simplified equivalent circuit for calculating mutual inductance.

Although several configurations are possible that involve overlap of the excitation signals, this section will only explore when the signals are not overlapping. This allows for the mutual inductances to be neglected. Also, it is reasonable to assume that the reluctances away from the point of contact are high when compared to the reluctances close to the point of contact.

Using the assumptions made above self inductances in terms of theta can be calculated as:

$$L_{11} = \frac{N^2}{R_{g1}} = \frac{\mu_o A_g N^2}{2r_{sr}\sin^2(\frac{\theta}{2})} \tag{3.26}$$

$$L_{22} = \frac{N^2}{R_{g2}} = \frac{\mu_o A_g N^2}{2r_{sr}\sin^2(\frac{\theta}{2} - \frac{\pi}{4})} \tag{3.27}$$

$$L_{33} = \frac{N^2}{R_{g3}} = \frac{\mu_o A_g N^2}{2r_{sr}\sin^2(\frac{\theta}{2} - \frac{\pi}{2})} \tag{3.28}$$

$$L_{44} = \frac{N^2}{R_{g4}} = \frac{\mu_o A_g N^2}{2r_{sr}\sin^2(\frac{\theta}{2} - \frac{3\pi}{4})} \tag{3.29}$$

The total energy and electromagnetic torque are as follows:

$$W_e = L_{11}i_1^2 + L_{22}i_2^2 + L_{33}i_3^2 + L_{44}i_4^2 \tag{3.30}$$

$$T_e = \frac{dW_e}{d\theta} = \Delta T_1 i_1^2 + \Delta T_2 i_2^2 + \Delta T_3 i_3^2 + \Delta T_4 i_1^2 \tag{3.31}$$

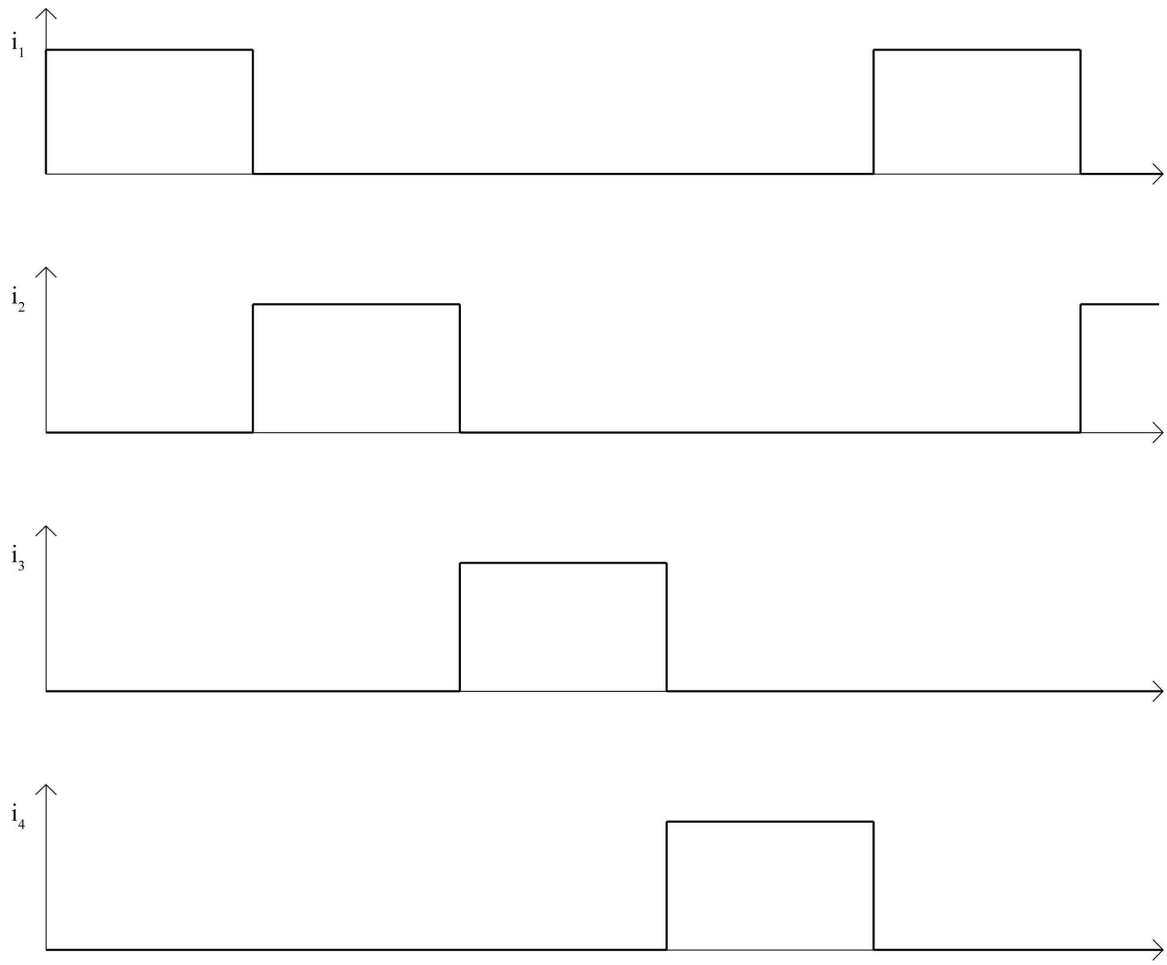

Fig. 3.7. Pole excitation signals.

Where ΔT_1, ΔT_2, ΔT_3, and ΔT_4 are:

$$\Delta T_1 = \frac{\mu_o A_g N^2 \tan\left(\frac{\theta}{2}\right) \sec^2\left(\frac{\theta}{2}\right)}{2r_{sr}} \tag{3.32}$$

$$\Delta T_2 = \frac{\mu_o A_g N^2 \tan\left(\frac{\theta}{2} - \frac{\pi}{4}\right) \sec^2\left(\frac{\theta}{2} - \frac{\pi}{4}\right)}{2r_{sr}} \tag{3.33}$$

$$\Delta T_3 = \frac{\mu_o A_g N^2 \tan\left(\frac{\theta}{2} - \frac{\pi}{2}\right) \sec^2\left(\frac{\theta}{2} - \frac{\pi}{2}\right)}{2r_{sr}} \tag{3.34}$$

$$\Delta T_4 = \frac{\mu_o A_g N^2 \tan\left(\frac{\theta}{2} - \frac{3\pi}{4}\right) \sec^2\left(\frac{\theta}{2} - \frac{3\pi}{4}\right)}{2r_{sr}} \tag{3.35}$$

This can be expanded into general terms for a machine with an n number of poles. In this case, the reluctances seen at pole k, R_{eqk} and R_{totk} are given as:

$$R_{eqk} = \left(\sum_{j=1}^{n} \frac{1}{R_{gj}} - \frac{1}{R_{gk}} \right)^{-1} \tag{3.36}$$

$$R_{totk} = R_{gk} + R_{eqk} \tag{3.37}$$

Using the same assumptions as above, the self inductance of pole k is found as:

$$L_{kk} = \frac{N^2}{R_{gk}} = \frac{\mu_o A_g N^2}{2r_{sr} \sin^2\left(\frac{\theta}{2} - \frac{(k-1)\pi}{n}\right)} \tag{3.38}$$

The total energy and electromagnetic torque of the machine becomes:

$$W_e = \sum_{j=1}^{n} L_{jj}^2 i_j^2 \tag{3.39}$$

$$T_e = \frac{dW_e}{d\theta} \sum_{j=1}^{n} \Delta T_j i_j^2 \tag{3.40}$$

Where for a given pole k:

$$\Delta T_k = \frac{\mu_o A_g N^2 \tan\left(\frac{\theta}{2} - \frac{(k-1)\pi}{n}\right) \sec^2\left(\frac{\theta}{2} - \frac{(k-1)\pi}{n}\right)}{2r_{sr}} \tag{3.41}$$

4. MECHANICAL MODELING

The following chapter will give an overview of important characteristics of the airgapless motor from a different perspective, including mechanical speed, vector analysis for the static torque, energy in the system, and a brief discussion regarding tribology.

4.1 Mechanical Speed

Unlike most electric machines, where the mechanical speed of the device is a function of the electrical frequency and the number of poles, the mechanical speed of the airgapless motor is a function of the electrical frequency, the difference of the two radii, and the radius of the rotor.

Assuming that there is no slip, in one complete electrical revolution, the arc length representing the motion of the hypocycloid is simply the difference between the two circumferences.

$$\omega_e = \frac{\Delta\theta}{\Delta t} = \frac{2\pi r_{sr}}{t_m} \tag{4.1}$$

For one complete mechanical revolution, the rotor will have rotated once:

$$\omega_m = \frac{\Delta\theta}{\Delta t} = \frac{2\pi r_r}{t_e} \tag{4.2}$$

Relating (4.1) to (4.2) can yield an expression for the mechanical speed of the device compared to the electrical frequency and the geometry of the device:

$$\frac{2\pi r_r}{t_e} = \frac{2\pi}{r_{sr}} t_m \Rightarrow \omega_m = \frac{r_{sr}}{r_r}\omega_e \tag{4.3}$$

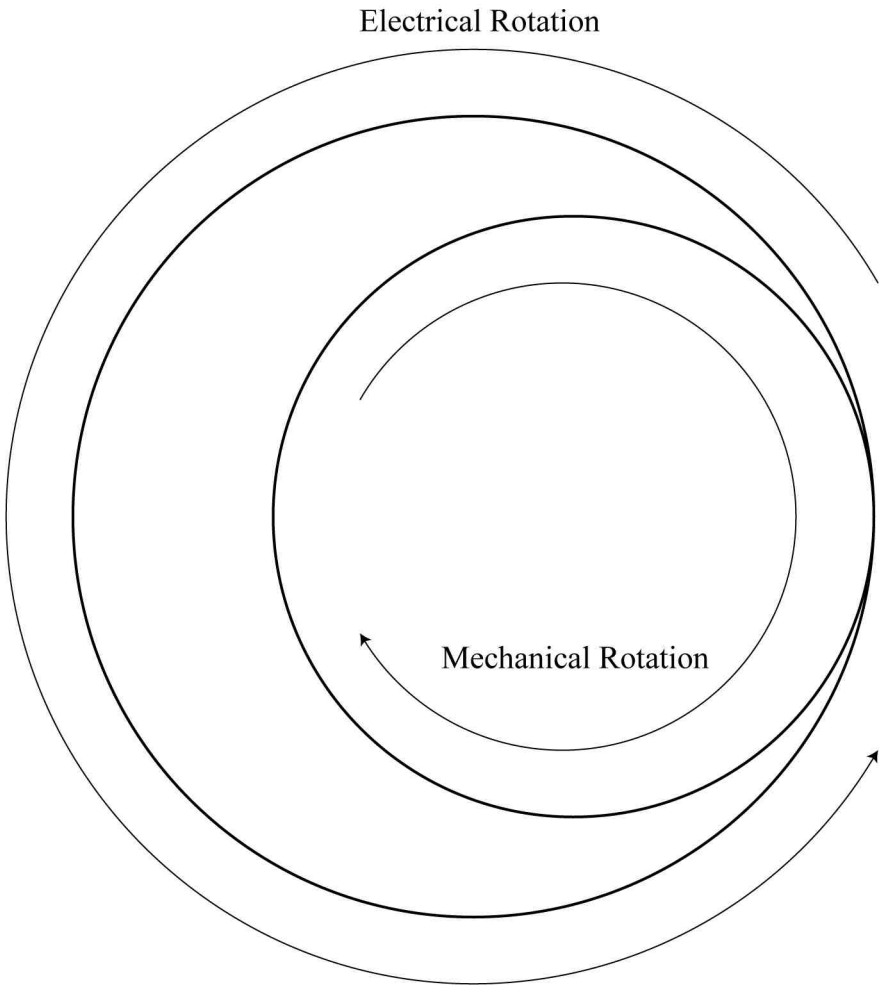

Fig. 4.1. Rotation of rotor about stator.

The time it takes for the hypocycloid to reach closure and return to its initial point can be found by using the initial parametric equations derived in chapter two as well:

$$x(\theta) = r_r \cos\left(\frac{r_{sr}}{r_r}\theta\right) + r_{sr}\cos(\theta) \tag{4.4}$$

$$y(\theta) = -r_r \sin\left(\frac{r_{sr}}{r_r}\theta\right) + r_{sr}\sin(\theta) \tag{4.5}$$

The starting point of the hypocycloid will be when $\theta = 0$. At this point the parametric equations become:

$$x(0) = r_r \cos(0) + r_{sr} \cos(0) = r_r + r_{sr} \tag{4.6}$$

$$y(0) = -r_r \sin(0) + r_{sr} \sin(0) = 0 \tag{4.7}$$

In order for the hypocycloid to close to its initial point, both the inputs of the trig functions must be some multiple of 2π. Therefore, the following should be true:

$$\frac{r_{sr}}{r_r}\theta = 2\pi, 4\pi, 6\pi... \tag{4.8}$$

Above, θ represents the electrical frequency. Using equation 4.5 it is possible to derive a simple expression to relate the mechanical and electrical speeds, which happens to be the same as (4.3)

$$\omega_m = \frac{r_{sr}}{r_r}\omega_e \tag{4.9}$$

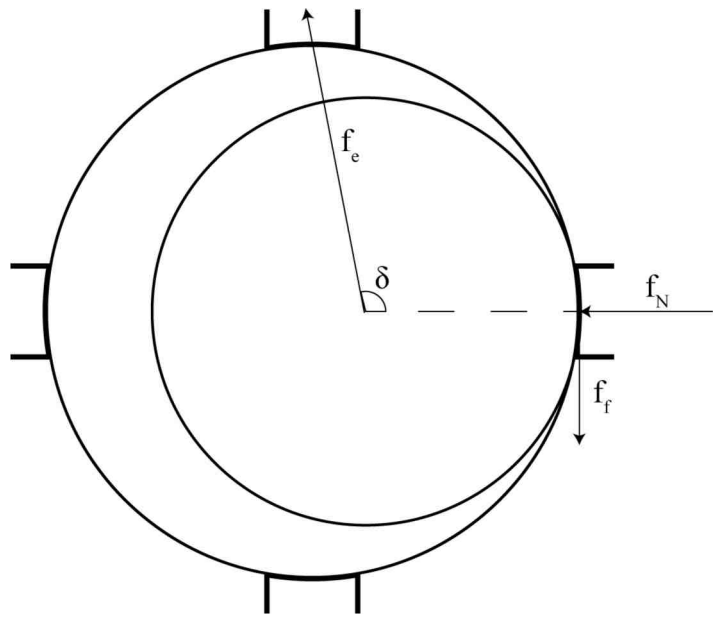

Fig. 4.2. Force diagram for airgapless motor.

4.2 Vector Analysis for Torque

Initially, an expression for the torque of a motor with a concept identical to the air gap-less motor was found by R. A. Ashten [12]. The basic torque expression derivation will be replicated below with the rotor being internal to the stator. This derivation assumes that the permeability of the material used for manufacturing is very high. This leads to the assumption that the flux lines will emerge from the rotor radially, which in turn leads to the action of the resulting electromagnetic force to be normal to the rotor. Refer to Fig. 4.2.

In Fig 4.2, f_e is the resultant magnetic force generated by the motor by activating the next pole. δ is the angle of action found in chapter 2. f_N is the normal force at the contact point, and f_f is the frictional force. In this example, the poles are excited in a counterclockwise direction, which causes the rotor itself to rotate in the clockwise direction. Since both the magnetic force and the frictional force are normal to the motor surface, the sum of torques can be found to be:

$$\tau = r_r f_f \tag{4.10}$$

Looking at the forces in the vertical direction and setting them equal to each other, the frictional force can be found as:

$$f_f = f_e \sin(\delta) \tag{4.11}$$

Where δ is the angle of action found in chapter two. Combining equations (4.10) and (4.11) yields a simple expression for torque in terms of the resultant magnetic force:

$$\tau = r_r f_e \sin(\delta) \tag{4.12}$$

Note that as the rotor reaches its point of contact at the active pole, that the expression for torque will reach zero.

It is important to quantify both the electromagnetic force f_e and the angle δ in terms of known quantities. The electromagnetic force f_e can be treated as if it were a relay. The derivation of f_e follows. Assuming that the flux density is uniform, the pole begins in an unmagnetized states, and that all the electrical energy is converted into mechanical energy, the total energy of the system can be given as:

$$W = \int_0^t \mathcal{E} i dt \tag{4.13}$$

Via Faraday's law, $\mathcal{E}$ is defined as the rate of change of magnetic flux.

$$\mathcal{E} = -N \frac{d\Phi_B}{dt} \tag{4.14}$$

Substituting (4.14) into (4.13) yields the following:

$$W = \int_0^t \mathcal{E} i dt = \int_0^t -N \frac{d\Phi_B}{dt} i dt = \int_0^\Phi -N i d\Phi_B \tag{4.15}$$

The magneto-motive force is defined as $\mathcal{F} = Ni = Hl$, where N is the number of turns on the coil, i is the current flowing through the coil, H is the magnetic field, and $g(\delta)$ is the length of the gap at an angle of δ. Substituting back into (4.15) yields the following:

$$W = \int_0^\Phi -N i d\Phi_B = \int_0^\Phi -H g(\delta) d\Phi_B \tag{4.16}$$

The magnetic flux Φ_B can be defined as the magnetic flux density B times the surface area through which the magnetic flux flows through A. Since $\Phi_B = AB$, $d\Phi = AdB$. Another substitution can be made to (4.16).

$$W = \int_0^\Phi H g(\delta) d\Phi_B = \int_0^B H g(\delta) A dB \tag{4.17}$$

Using the relationship that $B = \mu H$, more substitution and evaluation of the integral yields the following equation for the energy of the system.

$$W = \int_0^B H g(\delta) A dB = \int_0^B \frac{B g(\delta) A}{\mu} dB = \frac{B^2 g(\delta) A}{2\mu} \tag{4.18}$$

The permeability of the material is assumed to be much higher than that in the gap. Therefore, the above becomes.

$$W = \frac{B^2 g(\delta) A_g}{2\mu_o} \tag{4.19}$$

Where B is the magnetic flux density, $g(\delta)$ is the airgap length found in chapter two, A_g is the cross sectional area of the airgap, and μ_o is the permeability of air. The force on the rotor is the derivative of the total energy of the system with respect to the length of the gap.

$$f_e = \frac{dW}{dg}\frac{B^2 A_g}{2\mu_o} \tag{4.20}$$

As stated above, the magneto-motive force $\mathcal{F} = Ni = Hg(\delta) = \frac{Bg(\delta)}{\mu_o}$. Given this, it is possible to express f_e in known quantities.

$$f_e = \frac{\mathcal{F}^2 A_g \mu_o}{2g^2(\delta)} = \frac{N^2 i^2 A_g \mu_o}{2g^2(\delta)} \tag{4.21}$$

Where N is the number of turns in the coil, i is the current flowing through the coil, A_g is the effective cross sectional area of the gap, μ_0 is the permeability of air, and $g(\delta)$ is the length of the gap at the angle of action δ in chapter four.

for $\delta \leq 90°$, the angle of action δ is given as:

$$\delta = \pi - \sin^{-1}\left(\frac{r_s \sin\left(\frac{2\pi}{n}\right)}{x}\right) = \pi - \sin^{-1}\left(\frac{r_s \sin\left(\frac{2\pi}{n}\right)}{\sqrt{r_s^2 + r_{sr}^2 - 2r_s r_{sr}\cos\left(\frac{2\pi}{n}\right)}}\right) \tag{4.22}$$

When $\delta > 90°$, the action angle δ is given as:

$$\delta = \sin^{-1}\left(\frac{r_s \sin\left(\frac{2\pi}{n}\right)}{x}\right) = \sin^{-1}\left(\frac{r_s \sin\left(\frac{2\pi}{n}\right)}{\sqrt{r_s^2 + r_{sr}^2 - 2r_s r_{sr}\cos\left(\frac{2\pi}{n}\right)}}\right) \tag{4.23}$$

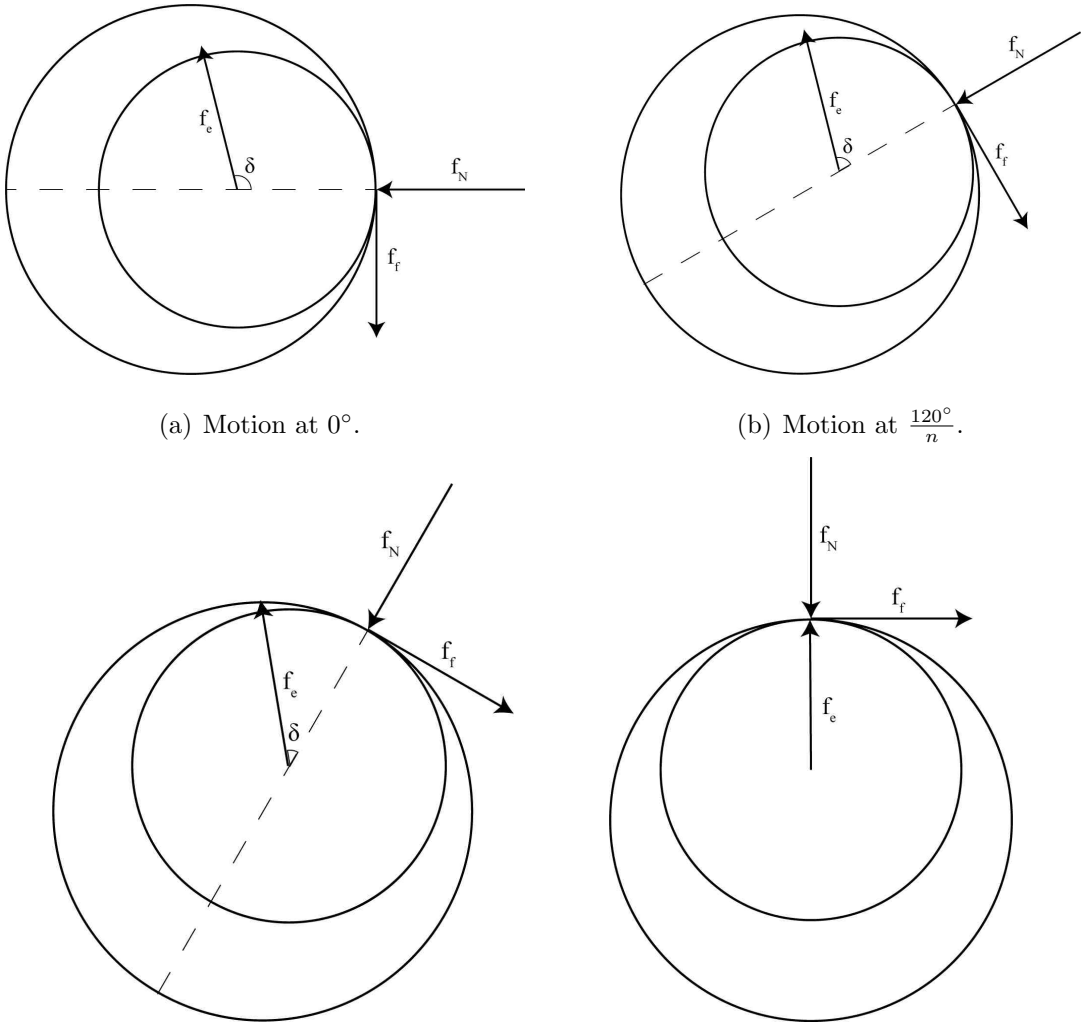

(a) Motion at 0°.

(b) Motion at $\frac{120°}{n}$.

(c) Motion at $\frac{240°}{3n}$.

(d) Motion at $\frac{360°}{n}$.

Fig. 4.3. Change of angle δ with respect to motion.

The frictional force f_f is the force that generates torque. This force is always tangential to the point of contact. It is worth noting that f_f is always normal to the angular position of the rotor θ. The force acting on the rotor due to the active pole is always normal to the rotor and directed towards the active pole of the stator. It is important then to develop a frame of reference for how the force vector f_e rotates with respect to the force vector f_f. This is similar to transforming the input variables

of a three phase device using reference frame theory [25] [26]. However, there are only two component forces to examine, so determining how f_e is rotating with respect to f_f is simple. Note Fig. 4.4 below.

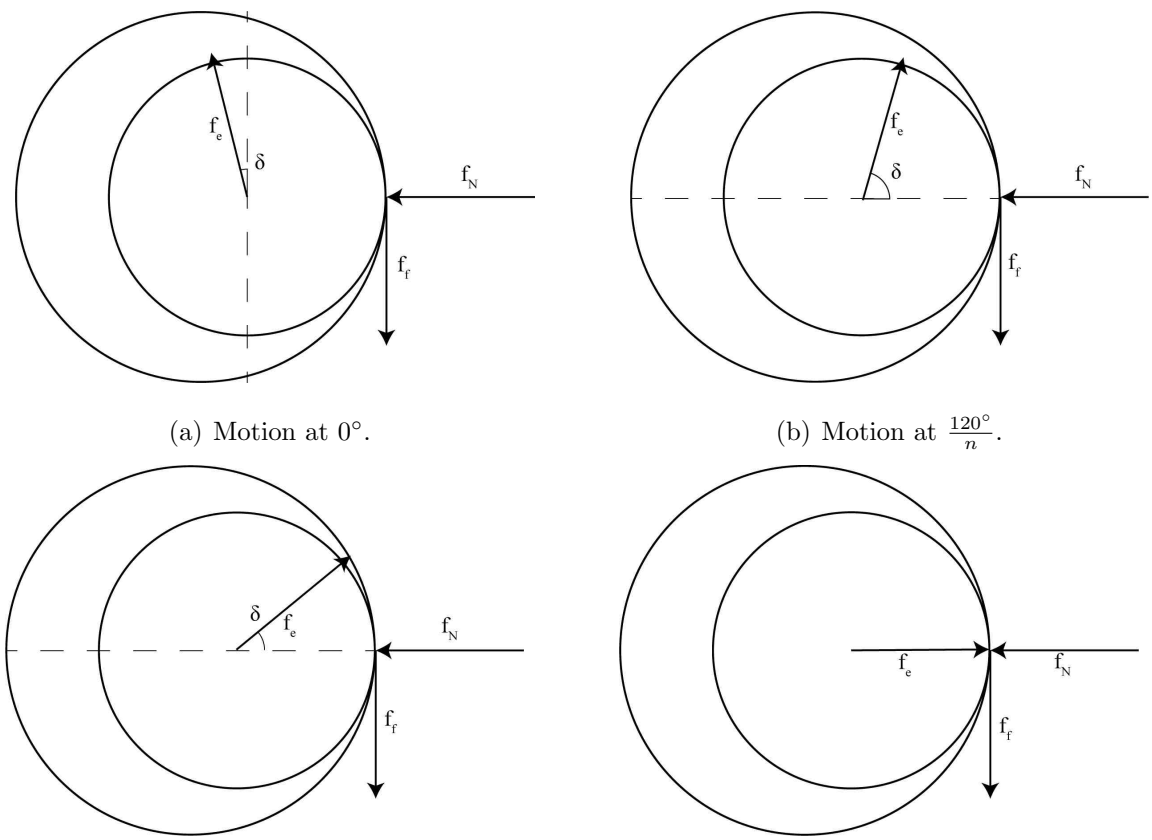

(a) Motion at 0°.

(b) Motion at $\frac{120°}{n}$.

(c) Motion at $\frac{240°}{n}$

(d) Motion at $\frac{360°}{n}$.

Fig. 4.4. Change of angle δ with respect to frictional force f_f.

For this analysis, it is assumed that the rotor is rotating without slip, and that the vector for the frictional force f_f will rotate at the same rate as the electrical frequency. That is:

$$\omega_{f_f} = \omega_e \tag{4.24}$$

As for the vector for the magnetic force generated by the active pole f_e, this vector approaches the next point of contact at the same rate. The velocity of the vector f_e can be given as:

$$\omega_{f_e} = \frac{\Delta\theta_(f)}{\Delta t} = \frac{\left(\frac{2\pi}{n}\right) - \delta}{\left(\frac{2\pi}{\omega_e}\right)} = \omega_e \left(\frac{1}{n} - \frac{\delta}{2\pi}\right) \tag{4.25}$$

Using (4.24) and (4.25), an expression for the torque τ at a function of time as it moves towards the next pole can be obtained.

$$\tau\left(t\right) = f_e\left(t\right) r_r \sin\left(\delta\left(t\right)\right) \tag{4.26}$$

For $0 \leq t \leq \frac{2\pi}{\omega_e n}$. Where $f_e\left(t\right)$ and $\delta\left(t\right)$ are:

$$f_e\left(t\right) = \frac{N^2 i^2 A_g \mu_o}{2g^2\left(\delta\left(t\right)\right)} = \frac{N^2 i^2 A_g \mu_o}{8 r_{sr}^2 \sin^4\left(\frac{\delta(t)}{2}\right)} \tag{4.27}$$

$$\delta\left(t\right) = \delta_n - \omega_e \left(\frac{1}{n} - \frac{\delta}{2\pi}\right) t - \omega_e t \tag{4.28}$$

The same analysis can be done for when there are two active poles. Consider Fig. 4.5. In this case, when the firing angle α is reached ($\theta = \alpha$), the second pole becomes active. In this case, There are two force vectors $f_{e1}\left(t\right)$ and $f_{e2}\left(t\right)$ and two angles of action $\delta_1\left(t\right)$ and $\delta_2\left(t\right)$. At $\theta = \alpha$, the two angles of action are given as:

$$\delta_1 = \sin^{-1}\left(\frac{r_s \sin\left(\frac{2\pi}{n} - \alpha\right)}{\sqrt{r_s^2 + r_{sr}^2 - 2 r_s r_{sr} \cos\left(\frac{2\pi}{n} - \alpha\right)}}\right) \tag{4.29}$$

$$\delta_2 = \sin^{-1}\left(\frac{r_s \sin\left(\frac{4\pi}{n} - \alpha\right)}{\sqrt{r_s^2 + r_{sr}^2 - 2 r_s r_{sr} \cos\left(\frac{4\pi}{n} - \alpha\right)}}\right) \tag{4.30}$$

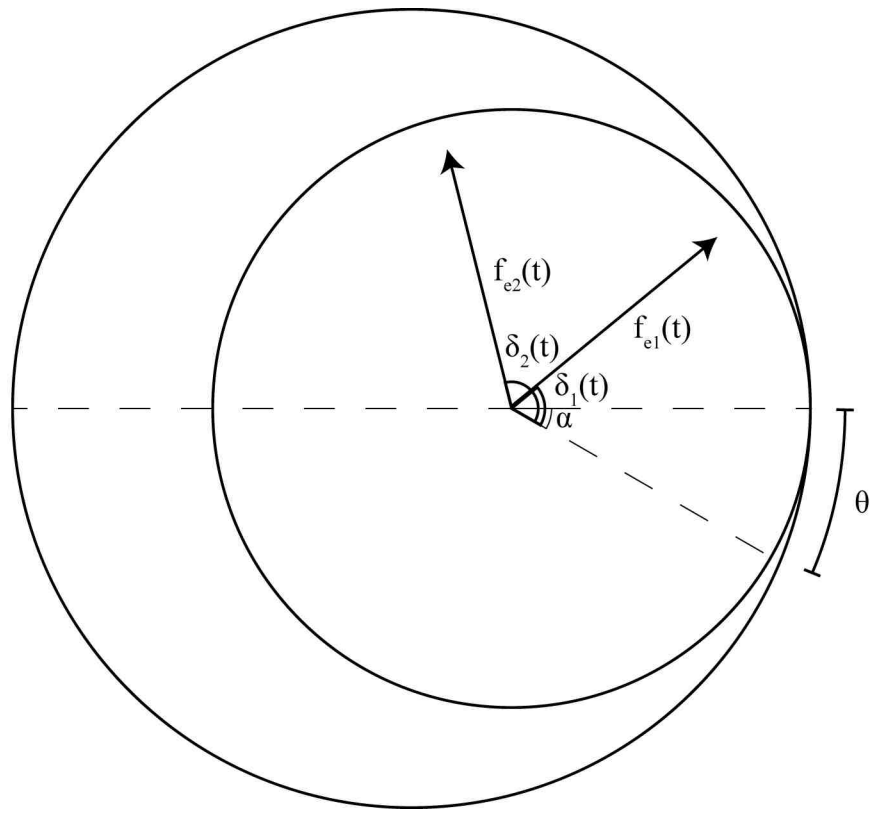

Fig. 4.5. Force diagram for airgapless motor with two active poles.

For $\delta_1, \delta_2 \leq \frac{\pi}{2}$ and:

$$\delta_1 = \pi - \sin^{-1}\left(\frac{r_s \sin\left(\frac{2\pi}{n} - \alpha\right)}{\sqrt{r_s^2 + r_{sr}^2 - 2r_s r_{sr}\cos\left(\frac{2\pi}{n} - \alpha\right)}}\right) \tag{4.31}$$

$$\delta_2 = \pi - \sin^{-1}\left(\frac{r_s \sin\left(\frac{4\pi}{n} - \alpha\right)}{\sqrt{r_s^2 + r_{sr}^2 - 2r_s r_{sr}\cos\left(\frac{4\pi}{n} - \alpha\right)}}\right) \tag{4.32}$$

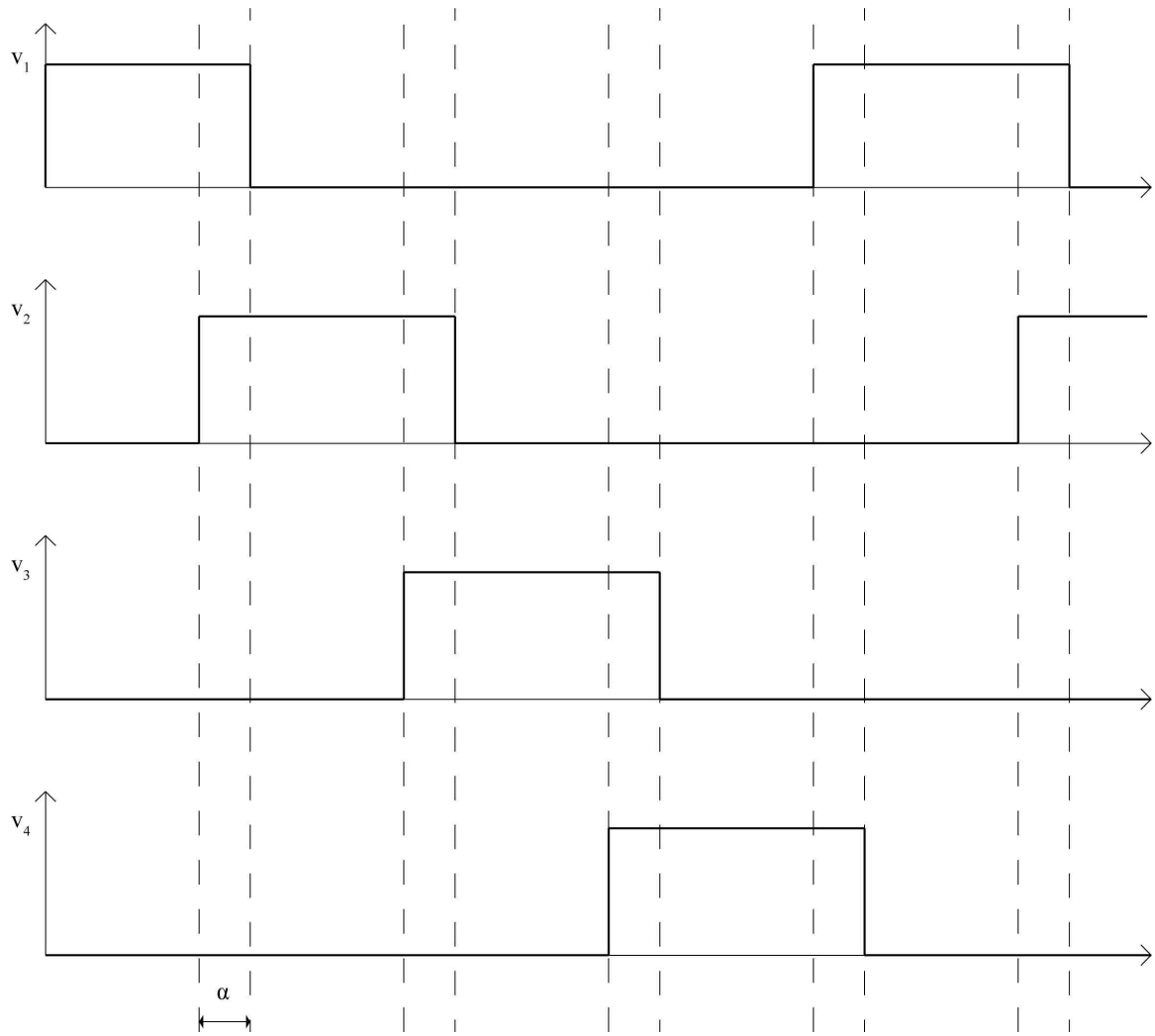

Fig. 4.6. Pole excitation signals with overlap angle of α.

For $\delta_1, \delta_2 > \frac{\pi}{2}$

The two forces at $\theta = \alpha$ are given as:

$$f_{e1} = \frac{N^2 i^2 A_g \mu_o}{2g^2\left(\delta_1\right)} = \frac{N^2 i^2 A_g \mu_o}{8 r_{sr}^2 \sin^4\left(\frac{\delta_1}{2}\right)} \tag{4.33}$$

$$f_{e2} = \frac{N^2 i^2 A_g \mu_o}{2g^2\left(\delta_2\right)} = \frac{N^2 i^2 A_g \mu_o}{8 r_{sr}^2 \sin^4\left(\frac{\delta_2}{2}\right)} \tag{4.34}$$

As with the example with one active pole, the friction force f_f is the force that generates torque. The friction force f_f is equal to the sum of the horizontal components with respect to the point of contact.

$$f_f = f_{e1} \sin(\delta_1) + f_{e2} \sin(\delta_2) \tag{4.35}$$

Making the same assumption above that the motor rolls without slipping at a constant angular velocity of $2\pi\omega_e$, then both δ_1 and δ_2 are closing on the point of contact with an angular velocity of:

$$\delta_1(t) = \delta_1 - \omega_e \left(\frac{1}{n} - \frac{\delta_1}{2\pi} \right) t - \omega_e t \tag{4.36}$$

$$\delta_2(t) = \delta_2 - \omega_e \left(\frac{2}{n} - \frac{\delta_2}{2\pi} \right) t - \omega_e t \tag{4.37}$$

From the above, it is possible to give a function for the torque as a function of time, just as was done with one pole.

$$\tau(t) = f_{e1}(t)\, r_r \sin(\delta_1(t)); \quad t < \frac{\alpha}{\omega_e} \tag{4.38}$$

$$\tau(t) = f_{e1}(t)\, r_r \sin(\delta_1(t)) + f_{e2}(t)\, r_r \sin(\delta_2(t)); \quad \frac{\alpha}{\omega_e} \leq t < \frac{2\pi}{n\omega_e} \tag{4.39}$$

4.3 Mechanical Energy

Energy in a mechanical system is defined at the sum of energies. As stated when addressing the geometry, there are two motions in this system to be concerned with: the rotation of the rotor about its own axis and the rotation of the rotor about the stator's axis. The total energy of this system can be written as:

$$E = \frac{1}{2} J_{sr} \omega_e^2 + \frac{1}{2} J_r \omega_m^2 \tag{4.40}$$

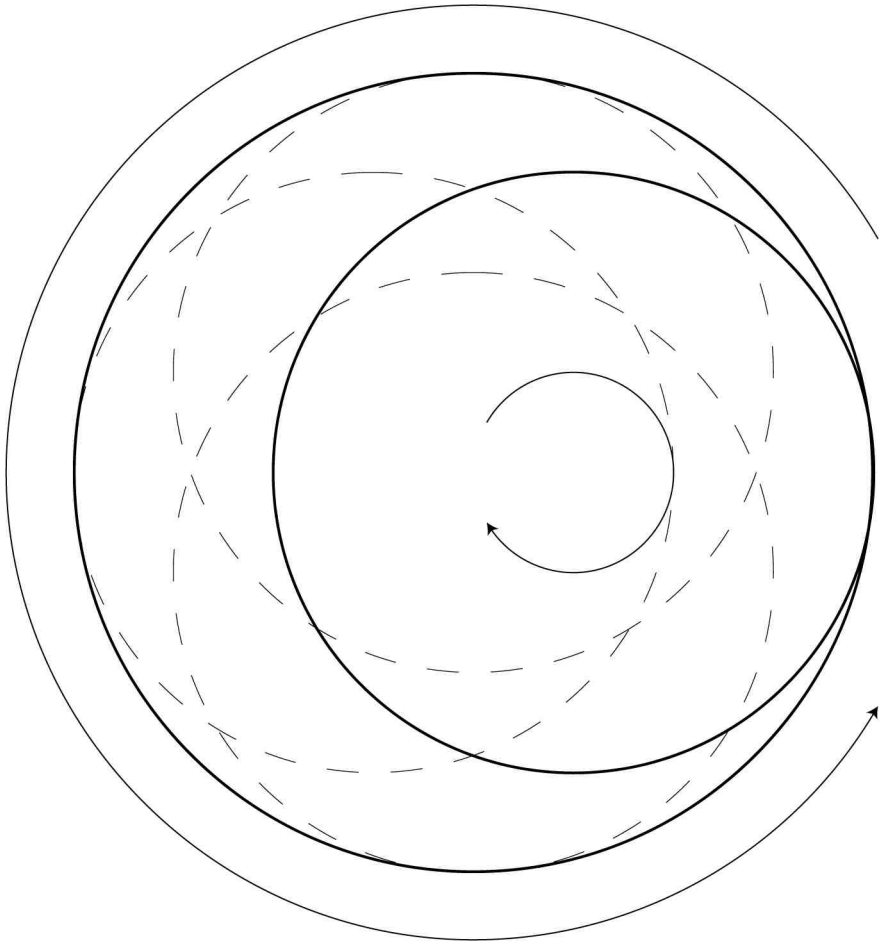

Fig. 4.7. Rotational and vibratory movement of airgapless motor.

Where J_{sr} is the moment of inertia of the rotor about the axis of the stator, and J_r is the moment of inertia about the rotor. These two values are quantified below:

$$J_{sr} = \frac{1}{2} m r_g^2 \approx \frac{1}{2} m r_{sr}^2 \tag{4.41}$$

$$J_r = \frac{1}{2} m r_r^2 \tag{4.42}$$

r_g is the radius of gyration of the rotor. Assuming no clearance between the stator and rotor, this value is approximately equal to the difference of the two radii r_{sr}. r_r is the radius of the rotor. Plugging in (4.6), (4.41), and (4.42) into (4.40) yields the total energy in the system:

$$E = \frac{1}{4} m r_{sr}^2 \omega_e^2 + \frac{1}{4} m r_r^2 \left(\frac{r_{sr}}{r_r} \right)^2 \omega_e^2 = \frac{1}{2} m r_{sr}^2 \omega_e^2 \tag{4.43}$$

4.4 Tribology

Tribology is known as the study and application of wear, friction, and lubrication. This concept is important to the airgapless motor as the amount of contact and reliance on friction as the provider of torque leads to issues with heat and wear to the device through extended use. Due to the relatively high frictional force on the point of contact, proper lubrication is recommended to cut down on the wear and heat generated at the point of contact.

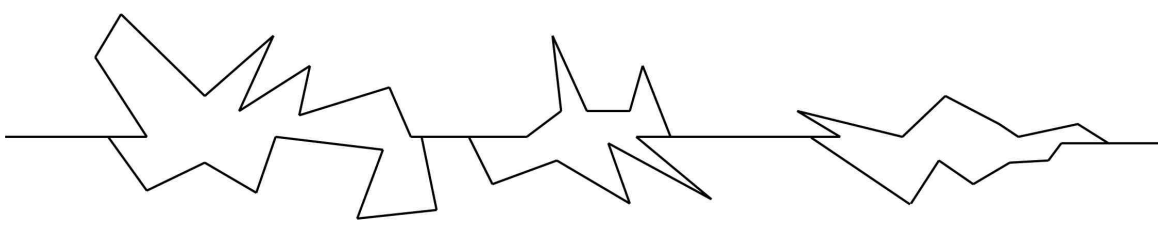

Fig. 4.8. Asperities between two surfaces in contact.

The type of rolling motion recommends that elasto-hydrodynamic lubrication is used. The value of λ can profoundly affect friction and cause the rotor to slip, which is undesirable. In order to select a lubricant, the lubricant film parameter λ, which is the measure of the effectiveness of the lubricant film, is used. The desired lambda constant is calculated as follows [27]:

$$\lambda = \frac{h}{\sigma} \tag{4.44}$$

Where h is the minimum film thickness, found either via a regression table or instrumentation, and σ is the composite root mean square roughness of the surfaces, defined as [28]:

$$\sigma = \sqrt{\sigma_s^2 + \sigma_r^2} \tag{4.45}$$

In production engineering, the value for h is often estimated to be between 0.9 and 1.1 microns. This should be sufficient for keeping abrasiveness of the two surfaces from contacting each-other, which significantly increases the lifespan of the device [29]. Attempts to quantify the appropriate value of h have been presented most recently by B. J. Hamrock and D. Dawson [30]. The Hamrock-Dawson formula is given as:

$$h_c \approx= k_h \left(2\left(r_s - r_r\right)\right)^{0.32} \left[\omega_e \left(r_s + r_r\right)\right]^{0.68} \eta^{0.68} G \tag{4.46}$$

Where k_h is the EHD film factor, η is the viscosity, and G is a material factor related to the surface of elasticity.

Below is a table of different types of lubrication and their respective value of λ [19].

Table 4.1.
Lubrication types with respective λ.

Hydrodynamic Lubrication	$5 < \lambda < 100$
Elasto-hydrodynamic Lubrication	$3 < \lambda < 10$
Partial Lubrication	$1 < \lambda < 5$
Boundary Lubrication	$\lambda < 1$

Note the action the wheel takes as it enters the point of contact. A closer view of this action is presented in Fig. 4.9. The above calculations have been done assuming there is no slipping between the rotor and the stator. However, because of the decrease in the cross section of the work taking place, there must be some sliding on the work relative to the roll, as well as minuscule changes to the direction of the friction vector f_f. The contact area is typically divided into three regions: one where the roll is greater than the work, one where the two move in unison, and one where the work is greater than the roll [29]. The theoretical analysis done in section 4.1 doesn't take these into account, as this slight change in the direction of the force of friction is considered negligible.

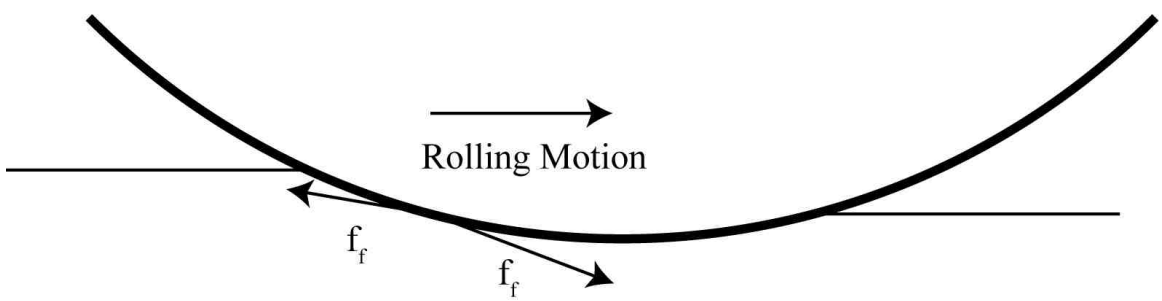

Fig. 4.9. Action of rolling wheel on surface.

Another consideration with regards to the Tribology of the device is the wear on the device over time. Unlike most electric machines, there is constant contact between the rotor and the stator, which makes wear and material selection a more important factor. A hydraulic device with a similar motion is a Gerotor pump. For a Gerotor without hydroelastic action, the wear on the device is governed by the Hertizan contact stress factor p_H, which is given by the following equation [31]:

$$P_H = \sqrt{\frac{F_i E*}{2\pi H R*}} \tag{4.47}$$

Where F_i is the contact force on the rotor at a given point, $E*$ is the reduced modulus of elasticity, H is the rotor thickness, and $R*$ is the composite value of the radius of curvature. A low stress factor is desirable when designing a device, so when choosing a material for the rotor of the device, a low modulus of elasticity is just as desirable as a low permeability.

5. CONTROL

5.1 Power Electronics

The airgapless motor uses a driver system that is similar to the driver for a switched reluctance motor. Although several circuits can be used for driving a switched reluctance motor, the most common is an asymmetric bridge converter.

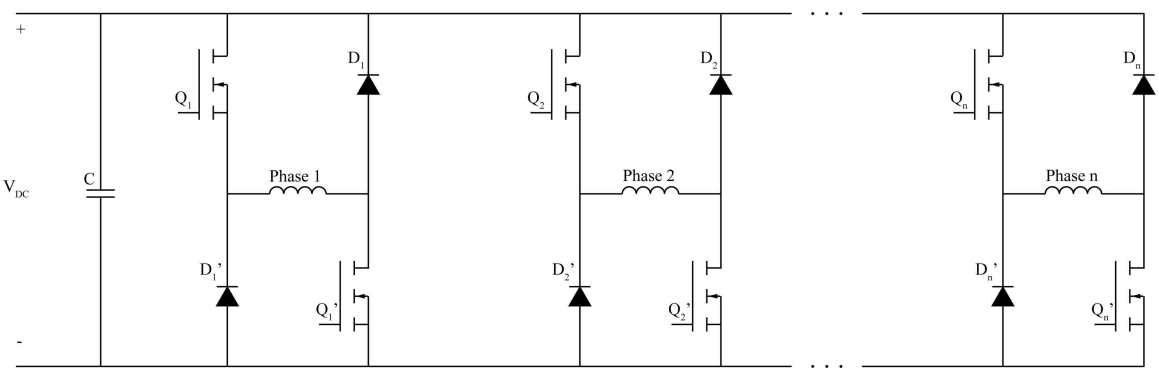

Fig. 5.1. Asymmetric bridge converter for driving airgapless motor.

Fig. 5.1 presents an Asymmetric Bridge Converter (ABC) for a motor with n-phases. When both switches on either side of a given phase is on, that pole is consider to be active, and the voltage across that given phase is V_{DC}. The placement of the diodes ensure that the current across the phase has path to discharge when either or both switches are inactive. Controllers for this specific application are available through Texas Instruments and NXP Semiconductor [32] [33]. The same type of power electronics circuit can be used to single leg of the converter along with a truth table are provided below [34] [35].

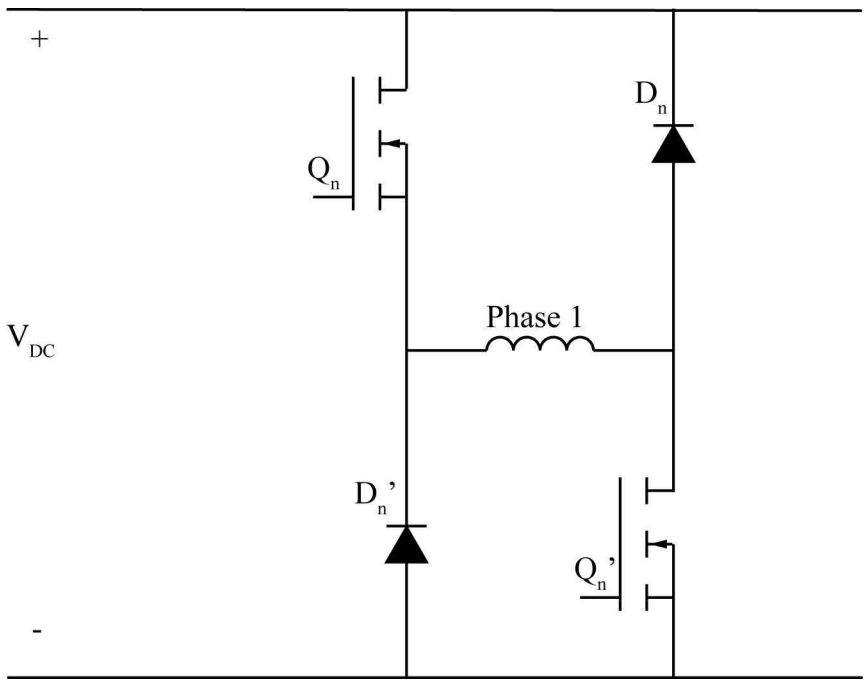

Fig. 5.2. One leg of asymmetric bridge converter for driving airgapless motor.

Table 5.1.
Truth table for asymmetric bridge converter.

q_n	q'_n	**Phase** n **Voltage**
0	0	0
0	1	0
1	0	0
1	1	V_{DC}

It is desirable to minimize the number of components in the power electronics circuit to reduce overall cost [36]. Below is another common power electronics circuit known as the (n+1) configuration. Rather than use two diodes for each phase, a single diode is used to allow current to flow out of the phase and back through the capacitor when Q_n is on and Q'_n is off. The switching strategy and truth table is identical to that of a normal configuration of an ABC.

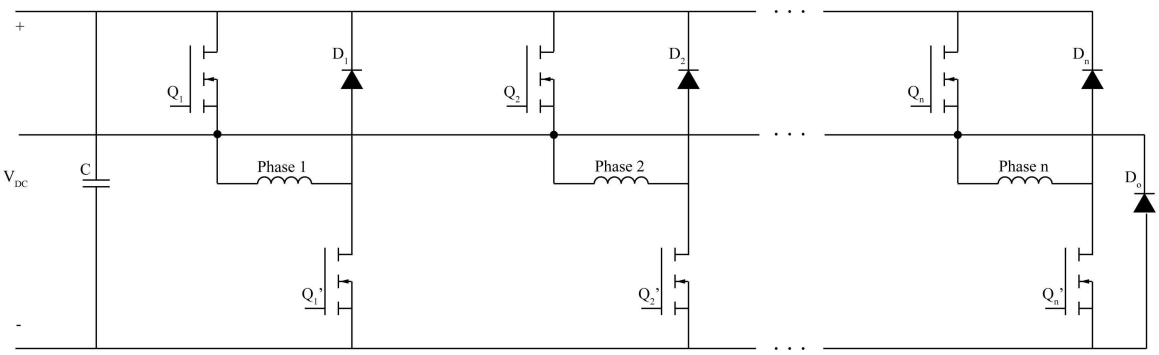

Fig. 5.3. Altered asymmetric bridge converter for driving airgapless motor.

5.2 Choosing an Overlap Angle

There are several unique methods for controlling the torque of a switched reluctance motor. These strategies include using a search algorithm to find the optimal firing angle to optimize efficiency and torque [37], using the mutual inductance of the device to derive an expression to minimize the torque ripple [38], and using a feedback controller to drive the motor with a specific reference current [39]. Most switched reluctance motors require a rigorous amount of feedback from the motor to operate at maximum efficiency with minimum vibrations [12] [40]. The same type of approach when operating with the air gap-less motor. The proposed diagram presented in Fig. 5.4. This generalized block diagram of the closed loop feedback controller uses the current to furnish a current profile that can minimize the torque ripple of the device. The position of the rotor is also used to control the firing angle in the case where there is overlap.

Both the tasks of maximizing the torque and minimizing the torque ripple prove to be complex problems via analytical calculations, both for choosing a firing angle α and reference current $i*_n$ can be found via feedback control and iterative search methods. There are several elegant one-dimensional search methods to find a value

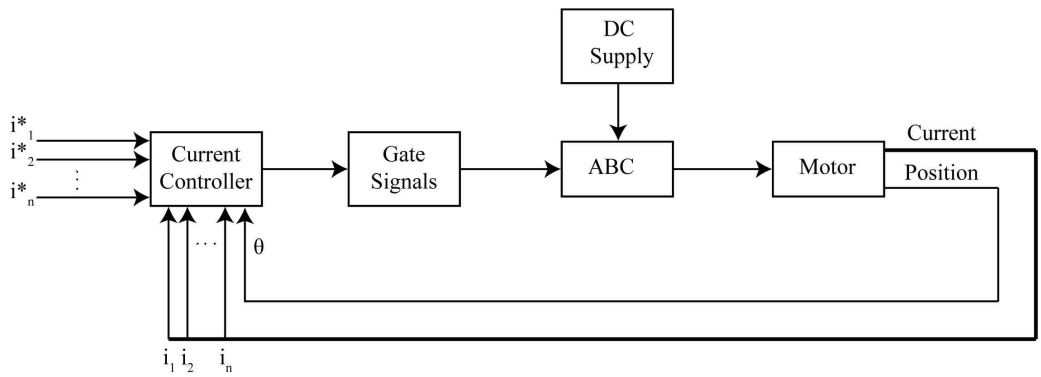

Fig. 5.4. Block diagram for feedback controller for airgapless motor.

for α that will either maximize the torque or minimize the ripple. A line search method is adopted via MATLAB to find an ideal value of α given the dimensions and specifications of the device [41].

Although it is difficult to derive the best value of α analytically for optimizing the average torque, it would make sense that having a large amount of overlap to maximize the friction force f_f would maximize the torque. Therefore, running with the maximum amount of overlap is how to accomplish the goal of maximizing the torque.

Minimizing the ripple can be more complicated. The torque is directly proportional to the current and indirectly proportional to the gap. Two strategies are suggested to minimize the torque ripple:

- Turn the off the kth pole and activating the $k+1^th$ pole before the kth pole makes contact with the rotor.

- Use pulse width modulation to taper the reference current down as the kth pole approaches its point of contact with the rotor.

6. SIMULATION AND RESULTS

6.1 Simulation

The following simulations were scripted in MATLAB. The inductance L, The angle of action δ, electromagnetic force f_e, and torque τ are all calculated iteratively. To more accurately simulate the inductive nature of the load in the power electronics circuit the current is calculated via Euler's method:

$$V = iR + L\frac{di}{dt}; \tag{6.1}$$

$$\Delta\left(i\right) = \Delta\left(t\right)\frac{V - iR}{L} \tag{6.2}$$

$$i_{k+1} = i_k + \Delta\left(i\right) \tag{6.3}$$

Values for the radius of the stator (r_s), number of turns(N), dc link voltage(V_{DC}, and coil resistance (R) are held constant. Table 6.1 shows the values used as constants.

Table 6.1.
Values used for simulation of airgapless motor.

Quantity	**Value**
Stator Bore Radius (r_s)	30cm
Number of Turns (N)	160
DC Link Voltage (V_{DC})	20V
Coil Resistance (R)	0Ω
Cross-Sectional Area of Pole (A_g)	4cm^2
Permeability of Air (μ_o)	$4\pi 10^{-7}$
Electrical Frequency (f_{fe})	60Hz

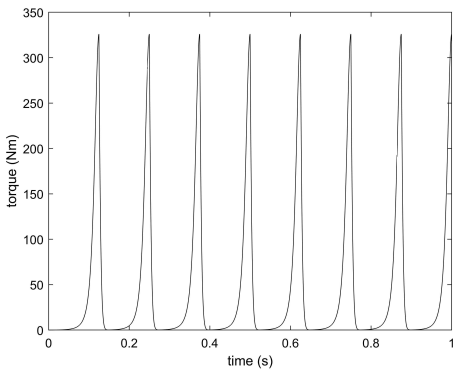

(a) Torque versus time.

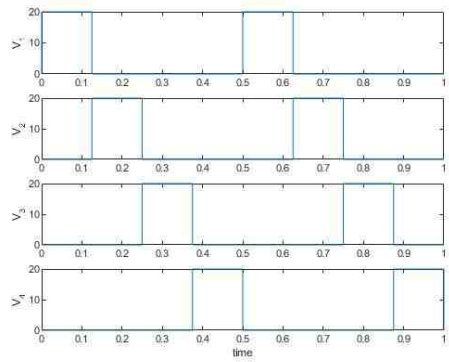

(b) V_{DC1-4} versus time.

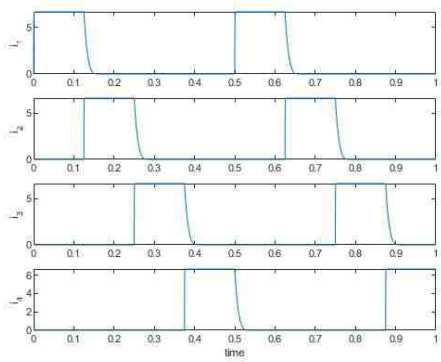

(c) I_{1-4} versus time.

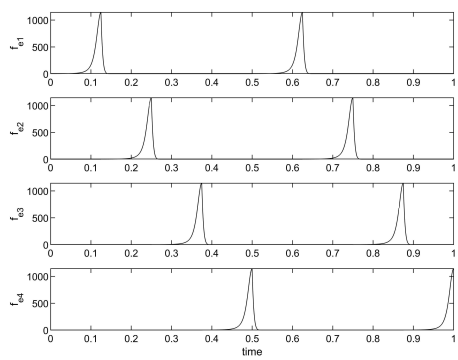

(d) f_{e1-4} versus time.

Fig. 6.1. Plots for $r_s : r_r = 15 : 14$, $n = 4$.

Fig. 6.1-6.4 shows the output of the static torque for values of static torque found in chapter 4, along with the phase voltages, phase currents, and phase forces. Values of $n = 4$ and $n = 6$ are both used, and the rotor is changed so that the ratio between the rotor and the stator bore radius is $r_s : r_r = 15 : 14$ and $r_s : r_r = 10 : 9$. For one electrical revolution, the torque peaks a total of n times, then goes back to it's lowest point as the contact pole is de-energized and the next pole is energized. Although the frequency of the device does not have much effect on the static torque, increasing the number of poles to a large value has a profound impact on the ripple while sacrificing average torque, as seen in Fig. 6.5.

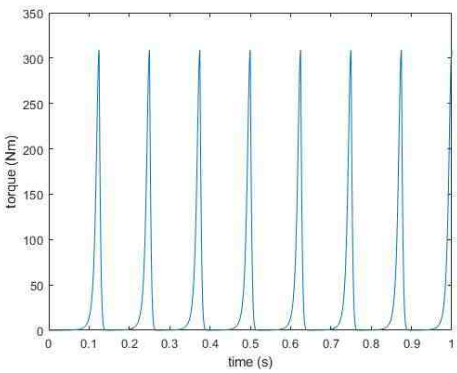

(a) Torque versus time.

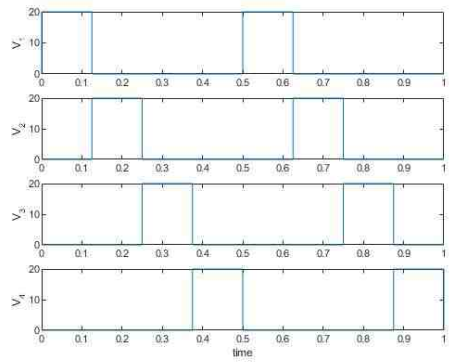

(b) V_{DC1-4} versus time.

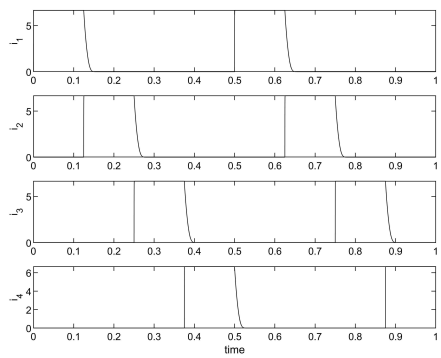

(c) I_{1-4} versus time.

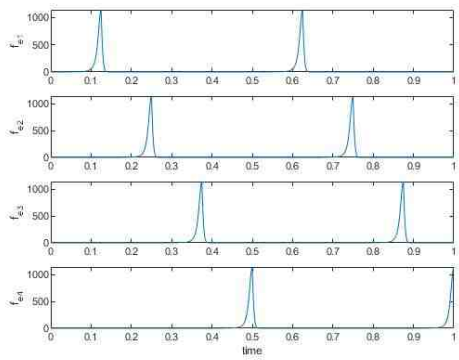

(d) f_{e1-4} versus time.

Fig. 6.2. Plots for $r_s : r_r = 10 : 9$, $n = 4$.

Next regarding insight gained by the firing angle α. In the developed model, changing the firing angle has little effect on the average torque and ripple, as shown in Fig. 6.6.

In Fig. 6.6, the overlap angle is changed from 0% overlap to 50% overlap for a six phase machine. Despite the drastic change of overlap, the average torque of the device does not significantly change. This is reasonable, as the force vector f_e is inversely proportional to the square of the gap, and the force generated by the next contact pole k is far greater than the force generated by the $k + 1^{th}$ pole. Fig 6.7 shows how the torque changes with respect to the firing angle and the input power.

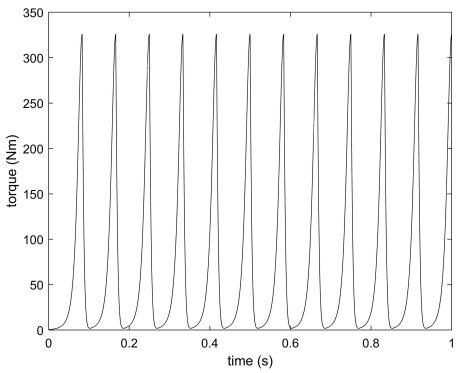

(a) Torque versus time.

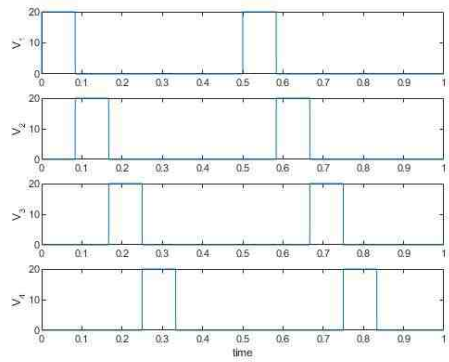

(b) V_{DC1-4} versus time.

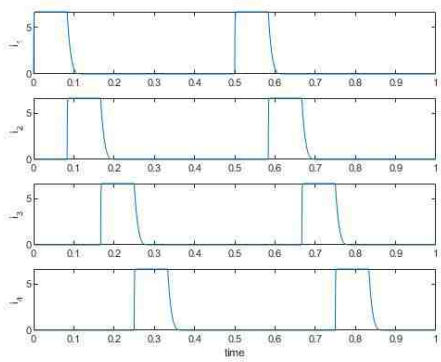

(c) I_{1-4} versus time.

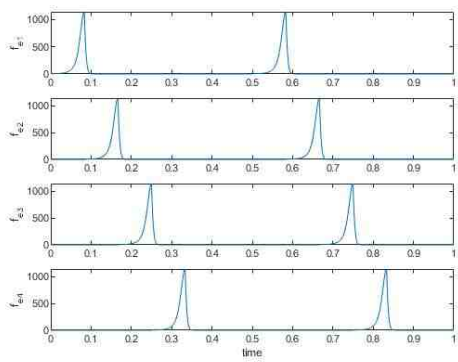

(d) f_{e1-4} versus time.

Fig. 6.3. Plots for $r_s : r_r = 15 : 14$, $n = 6$.

Fig. 6.8 attempts to use a reference current to alleviate the torque. The reference current is a sawtooth waveform. As the rotor approach the next contact pole, the current linearly increases to 0. This had two undesired effects. First, the torque waveform began to distort. This is likely due to the current through each phase distorting in an attempt to follow the reference current. The other undesired effect is the average torque becomes much lower than it would be with no reference current. This leads to the conclusion that using a gearing system or specialized shaft may be the most effective way to minimize ripple and vibrations.

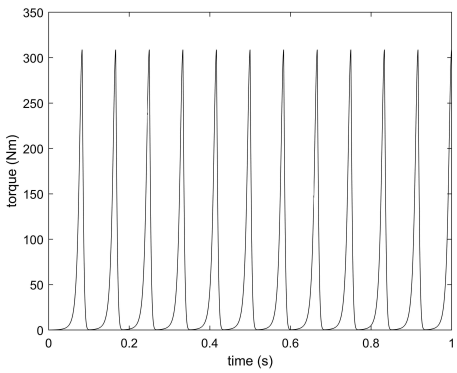

(a) Torque versus time.

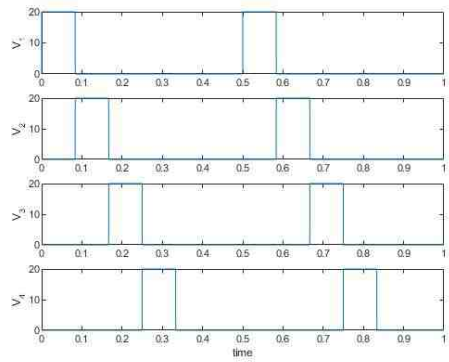

(b) V_{DC1-4} versus time.

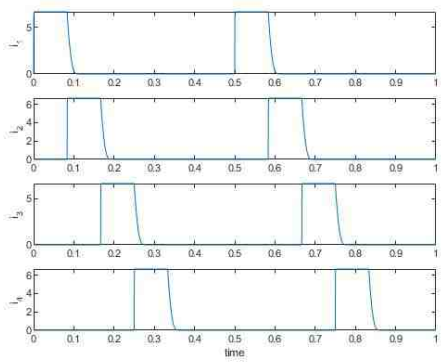

(c) I_{1-4} versus time.

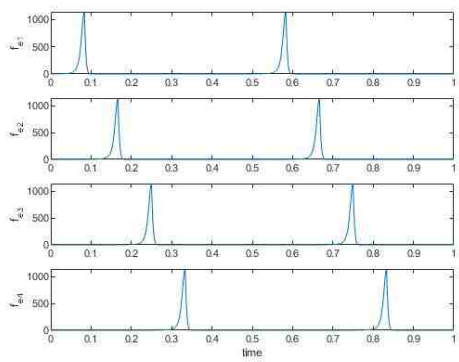

(d) f_{e1-4} versus time.

Fig. 6.4. Plots for $r_s : r_r = 15 : 14$, $n = 6$.

6.2 Prototypes

The device presented in Fig. 6.9 was developed in the ECE Power Electronics Lab. The rotor was machined to be a solid hollow cylinder of steel. The stator is a repurposed permanent magnet device salvaged from a household appliance. The stator was rewired in such a way that there were nine phases, two being fed to each coil. This function prototype exhibits behavior presented in the model developed.

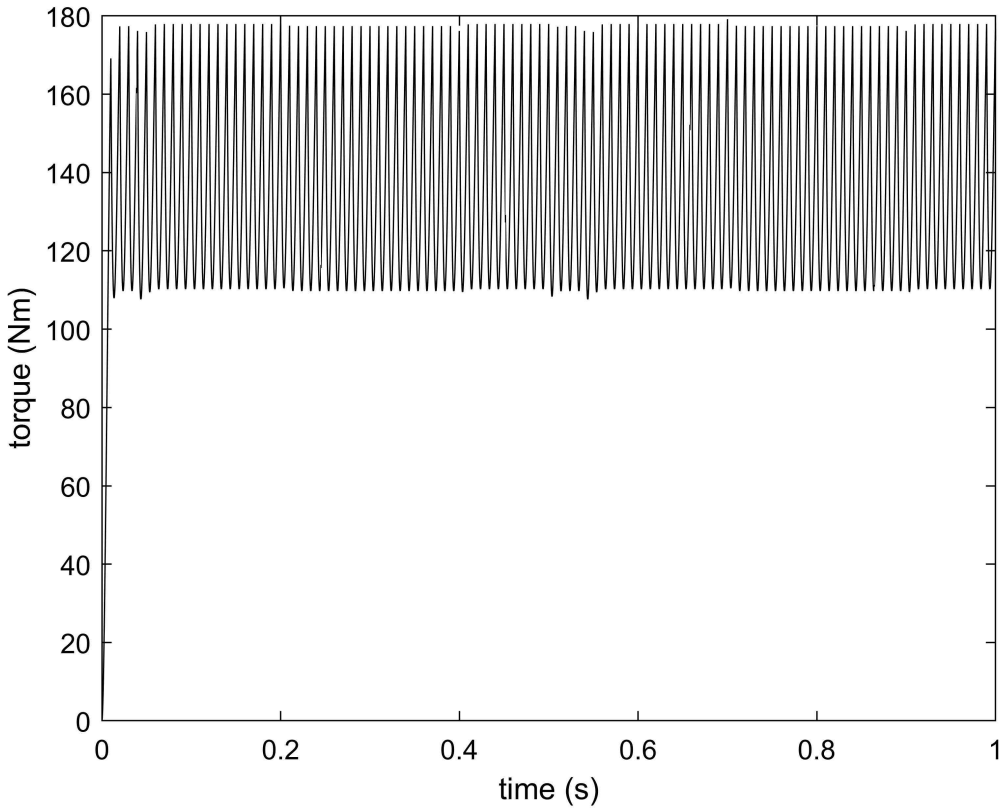

Fig. 6.5. Plot of torque versus time for $n = 50$.

Fig. 6.10 presents two other devices with the same concept. Fig. 6.10(a) shows a three phase prototype machines specifically for purpose of testing the concept of this device. Fig. 6.10(b) was a repurposed induction motor. The inner rotor was pulled from a different device.

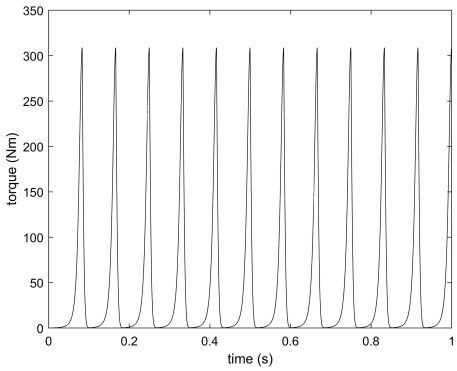

(a) $\alpha = 0$.

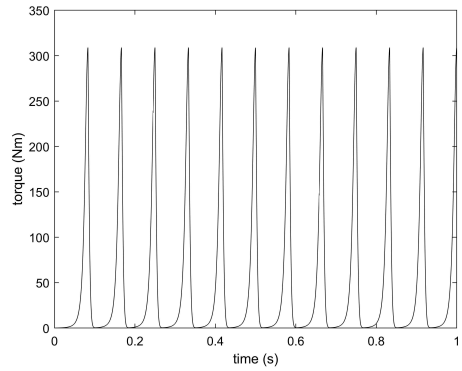

(b) $\alpha = \frac{180^\circ}{n}$.

Fig. 6.6. Torque for a 6 phase airgapless motor with varying firing angle α.

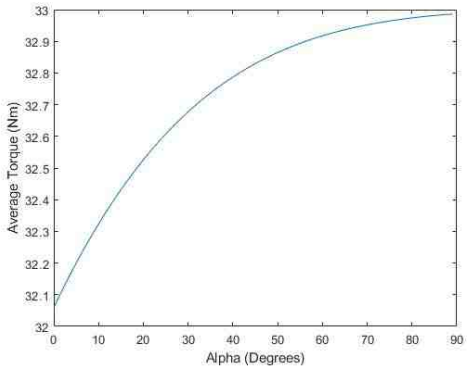

(a) Average torque versus firing angle.

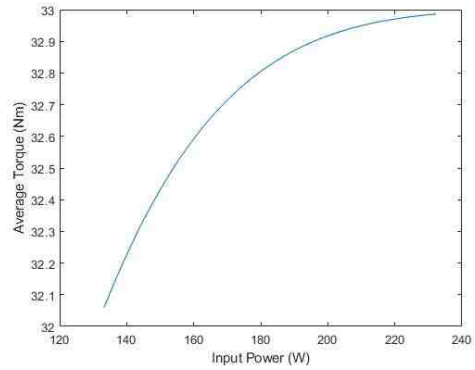

(b) Average torque versus input power.

Fig. 6.7. Torque versus firing angle and input power for varying firing angles.

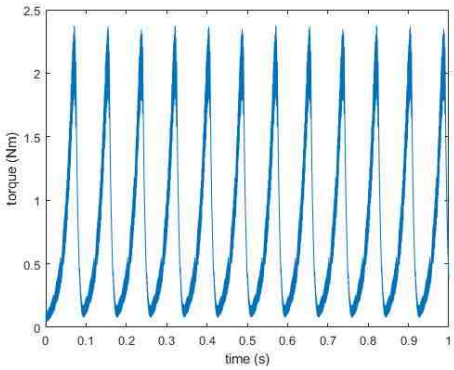

(a) Torque versus time.

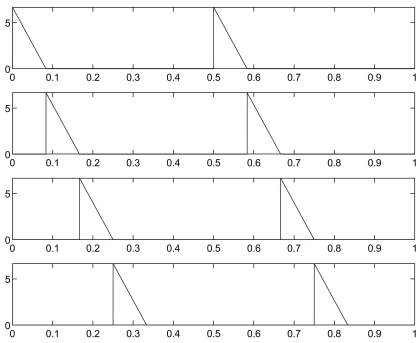

(b) V_{DC1-4} versus time.

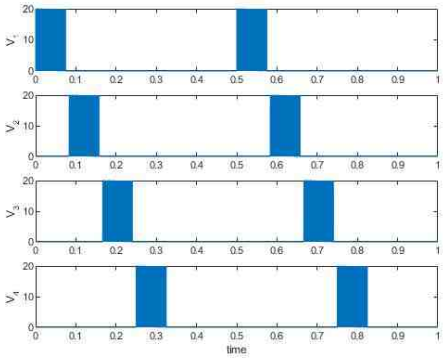

(c) I_{1-4} versus time.

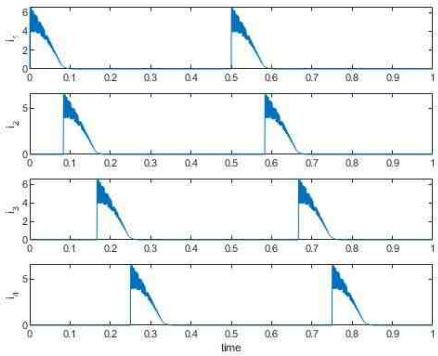

(d) f_{e1-4} versus time.

Fig. 6.8. Plots for torque, voltage, and current for six phase device and sawtooth reference current.

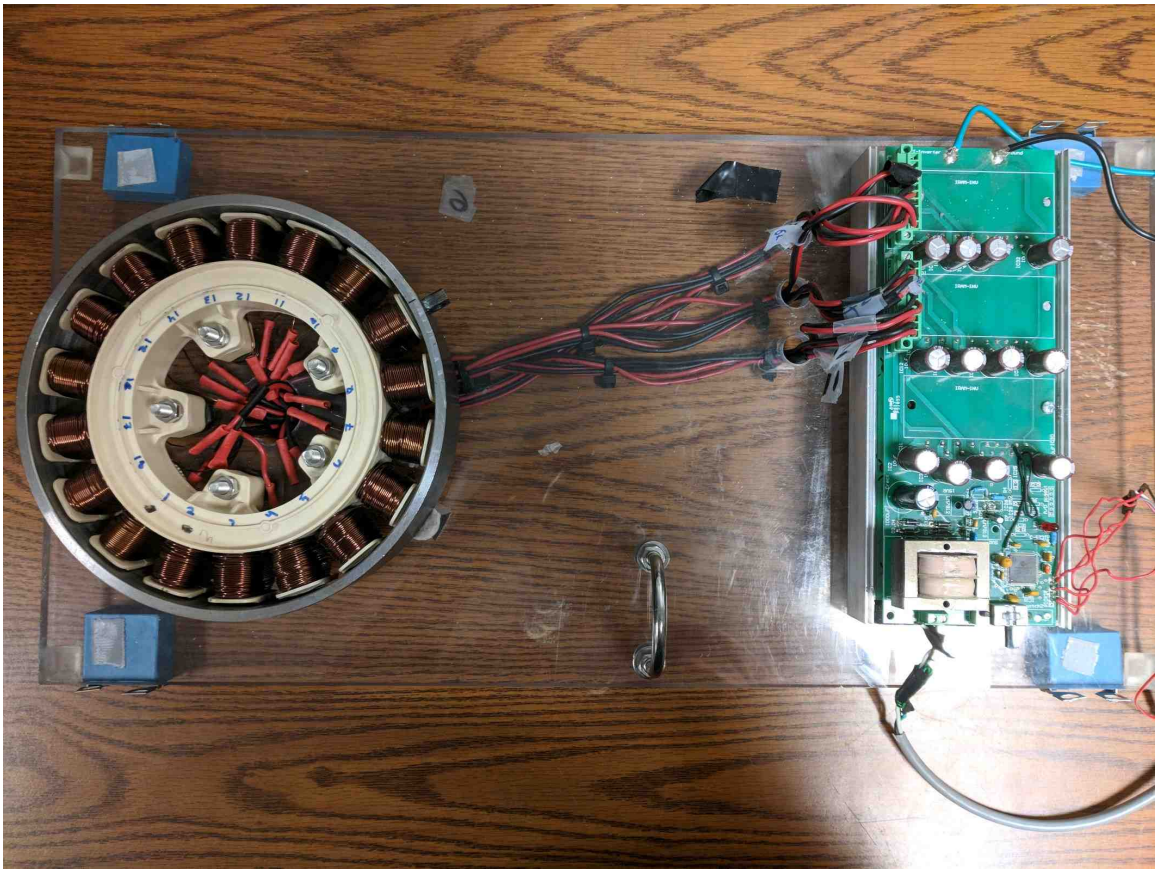

Fig. 6.9. Prototype motor with external rotor.

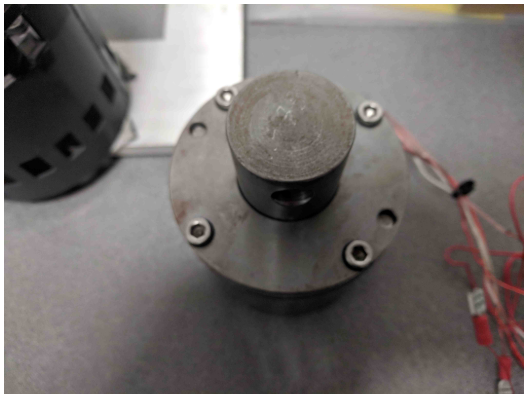

(a) Three phase internal rotor device.

(b) Multi phase internal rotor device.

Fig. 6.10. Multiphase internal rotor device.

7. SUMMARY

As advancements are made in power electronics and materials science it becomes more feasible to replace hydraulic machinery with electrical machinery. Thus, new designs, such as the airgapless motor, are being presented that offer functionality previously only seen in hydraulic machines. The airgapless motor presents new challenges to designers simply because of the non-intuitive nature of its motion. This paper presents a rough approach of how to model the airgapless motor through vector analysis. Comparatively, this approach synchronizes with the results seen in previous literature and prototypes of the device, and can furnish valuable information about driving the device to achieve maximum torque and minimum ripple. Although the model presented is fairly accurate, it is worth noting that several liberties were taken in obtaining it. Future research should include a more accurate model that accounts for slip and vibration, which could change the initial model significantly.

REFERENCES

REFERENCES

[1] S. Lee and J. Yun, "Influence of electrical steel characteristics on efficiency of industrial induction motors," in *2017 20th International Conference on Electrical Machines and Systems (ICEMS)*, August 2017, pp. 1–4.

[2] D. Lpez-Prez and J. Antonino-Daviu, "Application of infrared thermography to failure detection in industrial induction motors: Case stories," *IEEE Transactions on Industry Applications*, vol. 53, no. 3, pp. 1901–1908, May 2017.

[3] H. Nam, S.-K. Jung, G.-H. Kang, J.-P. Hong, T.-U. Jung, and S.-M. Baek, "Design of pole-change single-phase induction motor for household appliances," *IEEE Transactions on Industry Applications*, vol. 40, no. 3, pp. 780–788, May 2004.

[4] A. A. Kumar, G. R. Bindu, and D. Gopinath, "Performance analysis of single phase induction motor and switched reluctance motor used in domestic appliances with a view of energy conservation," in *2014 11th International Conference on Electrical Engineering/Electronics, Computer, Telecommunications and Information Technology (ECTI-CON)*, May 2014, pp. 1–6.

[5] T. Martire, D. Matt, and J. Fadar, "The permanent magnet synchronous motor in household appliances domain," in *2004 IEEE International Symposium on Industrial Electronics*, vol. 2, May 2004, pp. 1231–1235 vol. 2.

[6] M. Andriollo, M. D. Bortoli, G. Martinelli, A. Morini, A. Tortella, S. Bassini, and A. Scala, "Performance assessment of a single-phase pm synchronous motor for small fan appliances," in *2008 18th International Conference on Electrical Machines*, September 2008, pp. 1–6.

[7] R. Bayindir, I. Colak, E. Kabalci, and A. Gorgun, "Pid controlled synchronous motor for power factor correction," in *2009 International Conference on Power Engineering, Energy and Electrical Drives*, March 2009, pp. 408–412.

[8] A. E. Magri, F. Giri, A. Abouloifa, I. Lachkar, and F. Z. Chaoui, "Nonlinear control of associations including synchronous motors and ac/dc/ac converters: A formal analysis of speed regulation and power factor correction," in *2009 American Control Conference*, June 2009, pp. 3470–3475.

[9] A. S. Abdel-Khalik, A. M. Massoud, and S. Ahmed, "A senior project-based multiphase motor drive system development," *IEEE Transactions on Education*, vol. 59, no. 4, pp. 307–318, November 2016.

[10] B. S. R. Armstrong and Q. Yuan, "Multi-level control of hydraulic gerotor motors and pumps," in *2006 American Control Conference*, June 2006, pp. 8 pp.–.

[11] C.-S. Kim and C.-O. Lee, "Speed control of an overcentered variable-displacement hydraulic motor with a load-torque observer," *Control Engineering Practice*, vol. 4, no. 11, pp. 1563 – 1570, 1996. [Online]. Available: http://www.sciencedirect.com/science/article/pii/0967066196001700 (Last day accessed: June 4, 2018)

[12] R. A. Ashen and H. R. Bolton, "Aspects of the hypocycloidal reluctance motor," *IEE Proceedings B - Electric Power Applications*, vol. 128, no. 6, pp. 313–322, November 1981.

[13] A. Viviani, "Experimental and theoretical study of hypocycloidal motors with two-harmonic field windings," *IEEE Transactions on Power Apparatus and Systems*, vol. PAS-99, no. 1, pp. 292–300, January 1980.

[14] J. Reinert, J. H. R. Enslin, and E. D. Smith, "Digital control and optimization of a rolling rotor switched reluctance machine," *IEEE Transactions on Industry Applications*, vol. 31, no. 2, pp. 338–344, March 1995.

[15] M. Franke, M. Brutscheck, and U. Schmucker, "Modeling and simulation of a rolling rotor switched reluctance motor," in *2009 32nd International Spring Seminar on Electronics Technology*, May 2009, pp. 1–6.

[16] M. Franke, O. Punk, M. Brutscheck, and U. Schmucker, "Magnetic equivalent circuit modeling of rolling rotor switched reluctance motors," in *33rd International Spring Seminar on Electronics Technology, ISSE 2010*, May 2010, pp. 320–325.

[17] M. Franke, O. Punk, H. Mrech, and U. Schmucker, "Electrical actuation of a rolling rotor switched reluctance motor," in *Proceedings of the 2011 34th International Spring Seminar on Electronics Technology (ISSE)*, May 2011, pp. 451–456.

[18] M. Alibeik, O. Nezamuddin, M. Rubin, N. Wheeler, S. Silvestri, and E. dos Santos, "Airgap-less electric motor: A solution for high-torque low-speed applications," in *2017 IEEE International Electric Machines and Drives Conference (IEMDC)*, May 2017, pp. 1–8.

[19] M. Alibeik, O. N. M. Nezamuddin, R. M. Bagwe, M. J. Rubin, and E. C. dos Santos, "Airgapless electric motors with an external rotor," *IEEE Transactions on Industrial Electronics*, vol. 65, no. 9, pp. 6923–6935, September 2018.

[20] O. Nezamuddin, M. Alibeik, R. Bagwe, M. Rubin, and E. dos Santos, "Internal rotor airgap-less electric motors," in *2017 IEEE Energy Conversion Congress and Exposition (ECCE)*, October 2017, pp. 5009–5016.

[21] W. Zhang, G. Meng, and H. Li, "Electrostatic micromotor and its reliability," *Microelectronics Reliability*, vol. 45, no. 7, pp. 1230 – 1242, 2005. [Online]. Available: http://www.sciencedirect.com/science/article/pii/S0026271405000211 (Last day accessed: May 30, 2018)

[22] J. Stewart, *Calculus*. Brooks/Cole, 2012.

[23] S. D. Umans, *Fitzgerald's and Kingsley's Electric Machines*. Mcgraw Hill, 2014.

[24] P. Krause, O. Wasynczuk, S. Sudoff, and S. Pekarek, *Analysis of Electric Machinery and Drive Systems*. Wiley, 2013.

[25] P. C. Krause, O. Wasynczuk, S. D. Sudhoff, and S. Pekarek, *Reference-Frame Theory*. Wiley-IEEE Press, 2013, pp. 608–. [Online]. Available: https://ieeexplore.ieee.org/xpl/articleDetails.jsp?arnumber=6742738 (Last day accessed: June 1, 2018)

[26] P. C. Krause, O. Wasynczuk, and S. D. Pekarek, *Introduction to Reference-Frame Theory*. Wiley-IEEE Press, 2012, pp. 544–. [Online]. Available: https://ieeexplore.ieee.org/xpl/articleDetails.jsp?arnumber=6497265 (Last day accessed: June 1, 2018)

[27] E. V. Zarensky, "Bearing elastohydrodynamic lubricant: A complex calculation made simple," *NASA Technical Memorandum 102575*, April 1990.

[28] J. Guegan, A. Kadiric, A. Gabelli, and H. Spikes, "The relationship between friction and film thickness in ehd point contacts in the presence of longitudinal roughness," *Tribology Letters*, vol. 64, no. 3, p. 33, October 2016. [Online]. Available: https://doi.org/10.1007/s11249-016-0768-6 (Last date accessed: June 6, 2018)

[29] F. T. Barewell, "Tribology in production," *Production Engineer*, vol. 51, no. 7.8, pp. 253–261, July 1972.

[30] A. A. Lubrecht, C. H. Venner, and F. Colin, "Film thickness calculation in elasto-hydrodynamic lubricated line and elliptical contacts: The dowson, higginson, hamrock contribution," *Proceedings of the Institution of Mechanical Engineers, Part J: Journal of Engineering Tribology*, vol. 223, no. 3, pp. 511–515, 2009. [Online]. Available: https://doi.org/10.1243/13506501JET508 (Last day accessed: June 6, 2018)

[31] S.-M. KWON, M. S. KIM, and J.-H. SHIN, "Analytical wear model of a gerotor pump without hydrodynamic effect," *Journal of Advanced Mechanical Design, Systems, and Manufacturing*, vol. 2, no. 2, pp. 230–237, 2008.

[32] *Switched Reluctance Motor Control: Basic Operation and Example Using the TMS320F240*, Texas Instruments, February 2000.

[33] *3-Phase Switch Reluctance Motor Drive with Encoder Using 56F805*, NXP Semiconductors, March 2003, rev. 0.

[34] S. Ganguli, "Analysis of an asymmetric bridge converter for srm drives using pspice simulation," *International Journal of Advanced Engineering Technology*, vol. 2, no. 4, October-December 2011.

[35] M. Nashed, S. M. Mahmoud, M. Z. El-Sherif, and E. Sami, "Studying different types of power converters fed switched reluctance motor," vol. 1, pp. 281–290, December 2014.

[36] E. Afjei, A. Siadatan, and M. Rafiee, "Construction of a low cost asymmetric bridge converter for switched reluctance motor drive," in *2013 21st Iranian Conference on Electrical Engineering (ICEE)*, May 2013, pp. 1–5.

[37] J. H. Fisch, Y. Li, P. C. Kjaer, J. J. Gribble, and T. J. E. Miller, "Pareto-optimal firing angles for switched reluctance motor control," in *Second International Conference On Genetic Algorithms In Engineering Systems: Innovations And Applications*, September 1997, pp. 90–96.

[38] H.-K. Bae and R. Krishnan, "A novel approach to control of switched reluctance motors considering mutual inductance," in *2000 26th Annual Conference of the IEEE Industrial Electronics Society. IECON 2000. 2000 IEEE International Conference on Industrial Electronics, Control and Instrumentation. 21st Century Technologies*, vol. 1, 2000, pp. 369–374 vol.1.

[39] L. Du, B. Gu, J. S. J. Lai, and E. Swint, "Control of pseudo-sinusoidal switched reluctance motor with zero torque ripple and reduced input current ripple," in *2013 IEEE Energy Conversion Congress and Exposition*, September 2013, pp. 3770–3775.

[40] W. Cai and P. Pillay, "Design and control of switched reluctance motors with low vibration and noise," in *2007 IEEE International Electric Machines Drives Conference*, vol. 2, May 2007, pp. 1324–1331.

[41] E. K. P. Chang and S. H. Zak, *An Introduction to Optimization*. Wiley, 2013.